NUMERICAL INVESTIGATION AND EXPERIMENTAL VALIDATION OF PRIMARY FLOW NOZZLE OF AN EJECTOR SYSTEM

A THESIS SUBMITTED TO
THE GRADUATE SCHOOL OF NATURAL AND APPLIED SCIENCES
OF
MIDDLE EAST TECHNICAL UNIVERSITY

BY

BERİL EMERCE

IN PARTIAL FULFILLMENT OF THE REQUIREMENTS
FOR
THE DEGREE OF MASTER OF SCIENCE
IN
MECHANICAL ENGINEERING

SEPTEMBER 2023

Approval of the thesis

NUMERICAL INVESTIGATION AND EXPERIMENTAL VALIDATION OF PRIMARY FLOW NOZZLE OF AN EJECTOR SYSTEM

submitted by **BERİL EMERCE** in partial fulfillment of the requirements for the degree of **Master of Science** i**n Mechanical Engineering, Middle East Technical University** by,

Prof. Dr. Halil Kalıpçılar
Dean, **Graduate School of Natural and Applied Sciences** _____

Prof. Dr. Sahir Arıkan
Head of the Department, **Mechanical Engineering** _____

Assist. Prof. Dr. Ali Karakuş
Supervisor, **Mechanical Engineering, METU** _____

Prof. Dr. M. Halûk Aksel
Co-Supervisor, **Aeronautical Engineering, UTAA** _____

Examining Committee Members:

Prof. Dr. Metin Yavuz
Mechanical Engineering, METU _____

Assist. Prof. Dr. Ali Karakuş
Mechanical Engineering, METU _____

Assist. Prof. Dr. Özgür Uğraş Baran
Mechanical Engineering, METU _____

Prof. Dr. Tahsin Çağrı Şişman
Astronautical Engineering, UTAA _____

Assist. Prof. Dr. Onur Baş
Mechanical Engineering, TEDU _____

Date: 05.09.2023

I hereby declare that all information in this document has been obtained and presented in accordance with academic rules and ethical conduct. I also declare that, as required by these rules and conduct, I have fully cited and referenced all material and results that are not original to this work.

Name Last name : Beril Emerce

Signature :

ABSTRACT

NUMERICAL INVESTIGATION AND EXPERIMENTAL VALIDATION OF PRIMARY FLOW NOZZLE OF AN EJECTOR SYSTEM

Emerce, Beril
Master of Science, Mechanical Engineering
Supervisor: Assist. Prof. Dr. Ali Karakuş
Co-Supervisor: Prof. Dr. M. Halûk Aksel

September 2023, 101 pages

Ejector-Diffuser system is one of the pragmatic methods to convert high-pressure energy into kinetic energy, which is used to entrain the low-pressure flow. Because of its many advantages, the ejector is a preferable system for different applications. The main objective of the ejector system is mixing primary and secondary flow. The mixing process is a complicated concept directly affecting performance.

In this thesis study, the effects of the primary flow nozzle on mixing and ejector performance are investigated. To increase mixing efficiency, the chevron nozzle is selected as a primary flow nozzle and studied numerically and experimentally. In this study, a chevron nozzle is examined to observe the effect on performance by comparing it with a circular nozzle. CFD analyses are performed with ANSYS Fluent for different mass flow raes and mixing duct lengths.

In the experiment process, a chevron is also tested at different mass flow rates and mixing duct length to validate the numerical results. It is expected to increase the vacuum effect due to chevron influence, and it causes a decrease in test chamber

pressure. The comparison is performed with a circular nozzle to understand the impact on the ejector-diffuser system.

Keywords: Primary Flow Nozzle, Mixing Efficiency, Ejector-Diffuser System, Vacuum Capacity, Entrainment Ratio

ÖZ

EJEKTÖR SİSTEMİNİN BİRİNCİL AKIŞ LÜLESİNİN SAYISAL İNCELENMESİ VE DENEYSEL DOĞRULANMASI

Emerce, Beril
Yüksek Lisans, Makina Mühendisliği
Tez Yöneticisi: Doç. Dr. Ali Karakuş
Ortak Tez Yöneticisi: Prof. Dr. M. Halûk Aksel

Eylül 2023, 101 sayfa

Ejektör-Difüzör, yüksek basınç enerjisini kinetik enerjiye dönüştüren pragmatik sistemlerden biridir. Dönüştürülen kinetik enerji, düşük basınçlı akışın sistemin içerisine daha çok sürüklenmesi için kullanılmaktadır. Ejektör, sahip olduğu birçok avantajı nedeniyle sektörde farklı uygulamalar için tercih edilmektedir. Ejektör sisteminin temel amacı, birincil akış ile ikincil akışın en verimli şekilde karıştırılmasıdır. İki farklı basınca sahip akışın karıştırılma işlemi karmaşık bir kavramdır ve ejektör performansı doğrudan etkilemektedir.

Bu tez çalışmasında birincil akış lülesinin karıştırma ve ejektör performansı üzerindeki etkileri incelenmiştir. Karıştırma verimini artırmak için birincil akış lülesi olarak şevron lüle seçilmiş ve şevron lüle hem sayısal hem de deneysel olarak incelenmiştir. Bu çalışmada, şevron lülesi dairesel lüle ile karşılaştırılarak şevronun performans üzerindeki etkisini incelenmiştir. Farklı debiler, ejektör-difüzör system uzunlukları için ANSYS Fluent ile HAD analizleri yapılmıştır.

Deney sürecinde, şevron lüle, farklı debilerde ve karışım kanalı uzunluklarında test edilmektedir. Şevron lüle sayesinde vakum etkisinin artması ve bu sebeple test odası

basıncında azalma görülmesi beklenmektedir. Ejektör-difüzör sistemi üzerindeki etkileri anlamak için dairesel bir lüle ile karşılaştırma yapılmaktadır.

Anahtar Kelimeler: Birincil Akış Lülesi, Karışım Verimi, Ejektör-Difüzör Sistemi, Vakum Kapasitesi, Sürüklenme Oranı

To my family . . .

ACKNOWLEDGMENTS

Firstly, I would like to express thanks to Assist. Prof. Dr. Ali Karakuş for his support during this thesis study. I'd like to express my deepest and special thanks to Prof. Dr. Mehmet Halûk Aksel for his support, guidance, and supervision during this thesis study. It was a great privilege and honor to have a chance to study under his guidance.

Also, I'd like to say special thanks to the Vice Principal of TÜBİTAK SAGE, Dr. Bülent Sümer, for sharing his experience and providing all kinds of convenience.

And a special thanks to the Chief of the Hypersonic Systems Division in TÜBİTAK SAGE, Mr. Bora Yazıcı, for his significant contributions and discussion on the subject and the experimental process.

I would like to say thanks to my colleagues, Mr. Halil Arslan, Mr. Mustafa Pelit, and Mr. Ozan Can Kocaman, for their support throughout my thesis study.

I would like to my dear friends Dilay Güleryüz, Gizem Saygılı, and Güneş Aksu for their love, caring, and endless support during this challenging period.

Lastly, I would like to express endless thanks to my family, Gülistan Emerce and Nur Ber Emerce, for always being there for me and incredible support during the preparation of this thesis. Without them, this thesis would not have been possible.

TABLE OF CONTENTS

LIST OF TABLES

TABLES

LIST OF FIGURES

FIGURES

LIST OF ABBREVIATIONS

CAD	Computer Aided Drawing
CFD	Computational Fluid Dynamics
DNS	Direct Numerical Simulation
ER	Entrainment Ratio
HATS	High Altitude Test System
HiSA	High Speed Aerodynamic
L/D	Length to Diameter Ratio
LES	Large Eddy Simulation equations (LES)
NXP	Nozzle Exit Plane
PR	Pressure Ratio
RANS	Reynolds-Averaged Navier-Stokes equations
RCF	Rho Central Foam

LIST OF SYMBOLS

b	Base length of each chevron
C_v	Specific gas constant
D	Diameter of the nozzle
e	Internal energy
H	Height of the chevron
k	Thermal conductivity
L	Length of the nozzle
M	Molecular weight of the gas
$\dot{m}_{\text{secondary}}$	Secondary mass flow rate
$\dot{m}_{\text{primary}}$	Primary mass flow rate
N	Number of chevrons
$P_{\text{secondary}}$	Inlet pressure of the secondary flow
P_{exit}	Outlet pressure of the ejector-diffuser system
P	Pressure in the suction area
P_b	Back pressure
R_u	The universal gas constant
P_c	Critical back pressure
T	Temperature
U_0	Initial velocity
ΔP	Difference between the inlet and outlet pressure

ρ	Density
μ	Viscosity
β	The chevron tip angle
Ω_s	Streamwise vortices
Ω_n	Spanwise vortices

CHAPTER 1

INTRODUCTION

An ejector is a mechanical system that converts the high-pressure energy of motive fluid into kinetic energy by combining the primary and secondary flows. A low-pressure secondary flow is entrained and compressed while the motive flow diminishes its pressure. The ejector system has no moving part. There is no seal, shaft, or packing, which eradicates the maintenance problems. That is why ejector has recently received much attention in various industries because of their simple structure, compact size, and reliable performance [1].

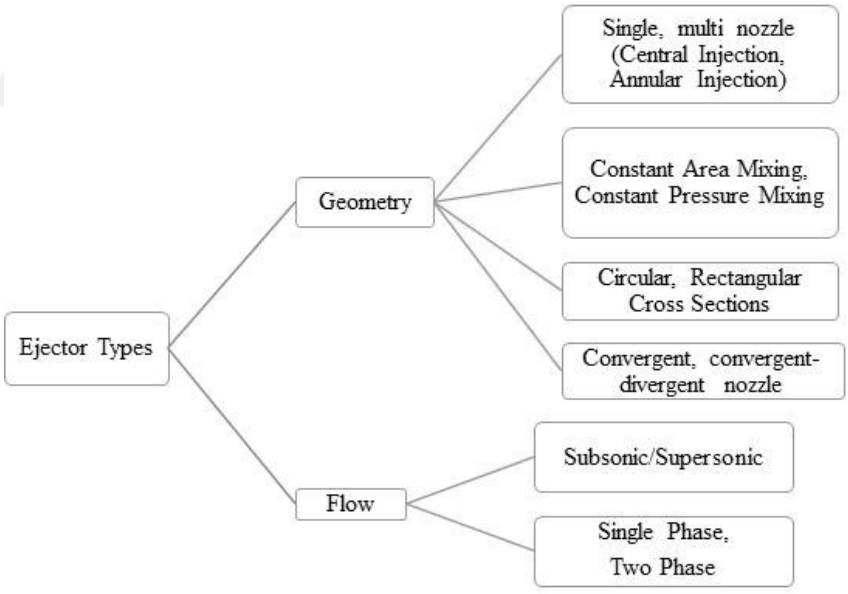

Figure 1-1 Ejector Types

According to internal flow characteristics and geometric configuration, ejector systems are mainly divided into two subcategories. The categories are represented in

Figure 1-1. As can be seen from Figure 1-1, the flow subcategory can be divided into subsonic or supersonic by considering the flow regime [2].

The other criteria to define the flow subcategory are based on the flow phases. The internal flow of the ejector can either be single-phase (gas-gas or liquid-liquid) or multiphase, relying on the primary and secondary flow phases. The single phase is a commonly chosen type because of its simplicity. Due to the variety of flow patterns, multiphase flow is substantially more complex than single-phase flow [3]. The physics behind it is related to phase change methodology. During the phase change process, the rapid changes in the flow characteristics bring about the shock wave, and it can be analyzed in detail using heat transfer and mixing phenomena [4].

In addition to their flow characteristics, ejectors are categorized according to their geometry. This topic can be treated under four headings: cross-section type, location of nozzle, nozzle type, and diffuser area. At first, cross-section geometry is one of the design parameters for an ejector, defined as a circular or rectangular cross-section, and the ejector is named according to that. The second geometry parameter is the location of the nozzle. According to the position of the nozzle, the ejector can be called a central or annular injection. Central ejectors are used in many applications. The axisymmetric ejector system injects the primary flow along the system's centerline, as shown in Figure 1-2.

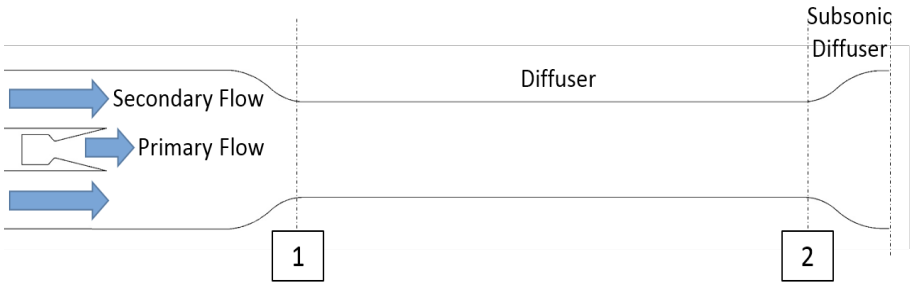

Figure 1-2 Central Injection Type [2]

Annular injection of the primary flow provides a practical solution to other types of injection, and it is a symmetric kind of system. The secondary flow passes the primary flow without significant disruption when the primary flow is injected by an

annular nozzle at the inside wall of the secondary flow duct, and it becomes an alternative ejector type [5].

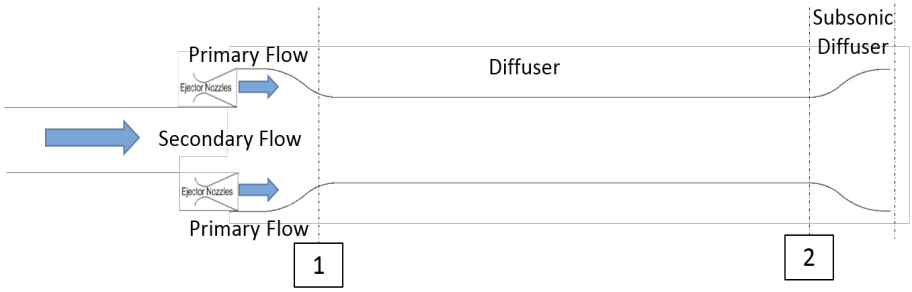

Figure 1-3 Annular Injection Type [2]

Nozzle design is the central issue of the ejector system. It modifies the whole system outputs. Nozzle geometry is designed by considering the characteristics of the flow regime and shock formation. A convergent nozzle is commonly preferred if the flow is subsonic, or the interface of the suction chamber and the mixing chamber has sonic flow. On the other hand, for supersonic ejectors, convergent-divergent nozzle type is generally chosen.

The diffuser section of the ejector can be designed in two different configurations: the constant area and the constant pressure ejector. The constant area ejectors have simple construction, but at the same time, strongly dissipated shock trains are observed, and there should be a high level of nozzle pressure to initiate the process inside the system. Constant area ejectors have a higher capacity to suck mass flow rate, but constant pressure ejectors can present more stable performance in varied back pressure ranges. For this reason, constant pressure ejectors become preferable.

1.1 The Working Principle of Ejector System

The mixing process is a complex phenomenon resulting from interactions between several gas dynamic phenomena, including shock waves and shear layers. The supersonic ejector-diffuser system includes the primary nozzle, the suction (mixing) chamber, the mixing duct, and the diffuser. The secondary flow is entrained when

the high-speed primary flow generates a low-pressure area. The secondary flow is compressed from its initial low-pressure state after interaction with the primary flow. Then, mixed flows move through the mixing duct, where the primary and secondary flows convert mass, momentum, and energy. A supersonic mixed flow is created by combining the two flows, colliding with re-compression shock structures in the mixing duct. Subsonic flow lastly exits the ejector through the diffuser, converting kinetic energy to pressure when it passes downstream of re-compression shock structures [7].

1.2 Ejector System Performance

The ejector performance can be specified in terms of three parameters: entrainment ratio, pressure recovery, and mixing efficiency. The most critical parameter is the entrainment ratio of an ejector-diffuser system because it verifies the system's performance in terms of vacuum capacity.

The higher the velocity of the jet leaving the ejector's nozzle, the higher the pressure it may exhale into, or, if the exit pressure is constant, the higher vacuum it would generate. The amount of entrainment is one of the performance factors of the system, and the entrainment ratio is calculated as [9].

$$ER = \frac{\dot{m}_{secondary}}{\dot{m}_{primary}} \tag{1.1}$$

The entrainment ratio affects the pressure recovery in the ejector-diffuser system and the vacuum capacity. The system could perform at higher pressures and accomplish greater compression since a high entrainment ratio can lead to faster pressure recovery. On the other hand, a low entrainment ratio may lead to a reduced pressure recovery, which restricts the system's operational range. Pressure recovery (ΔP) is defined as the difference between the inlet of the secondary flow ($P_{secondary}$) and the outlet of the ejector-diffuser system (P_{exit}).

$$\Delta P = P_{exit} - P_{secondary} \tag{1.2}$$

Another performance factor is related to mixing efficiency. The process of integrating two or more fluid flows into a homogenous mixture is referred to as mixing, and an ejector system's performance depends heavily on mixing. Further details about mixing will be explained in Section 1.4.

Based on the back pressure, the performance of the ejector can be classified into three operational modes, as illustrated in Figure 1-4 [8]. These modes are categorized based on the relationship between the pressure in the suction area (P), the back pressure (P_b), and the critical back pressure (P_c). The modes are identified as critical, subcritical, and back flow:

- Critical mode: If the entrainment ratio remains constant, the primary and secondary flows are both choked. $P \leq P_c$
- Subcritical mode: If only the primary flow is choked, the back pressure alters the entrainment ratio. The entrainment ratio ranges from zero to the critical entrainment ratio. $P_c<P\leq P_b$
- Back flow mode: When the entrained flow is reversed and neither the primary nor the secondary flow are choked. $P_b \leq P$ It can be noticed that in back-flow mode, the ejector entirely loses its functionality. Hence, critical, and subcritical modes essentially include the complete operational range.

The critical and subcritical modes encompass the entire operational range, and to achieve enhanced performance, the ejector should operate in the critical mode.

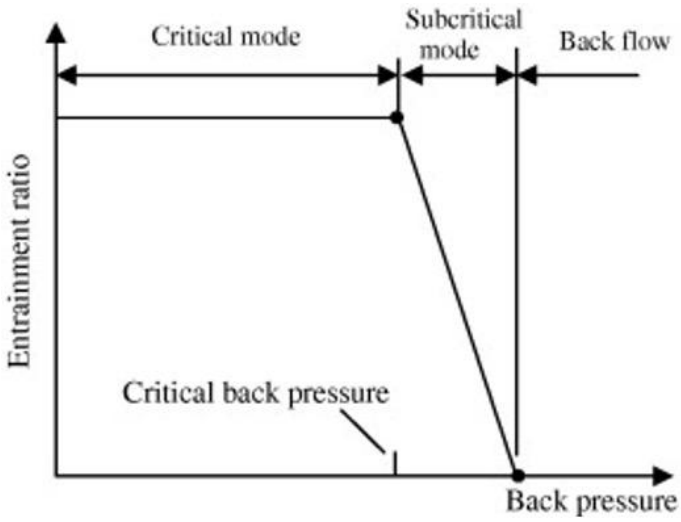

Figure 1-4 Operational modes [6]

1.2.1 Ejector Design Geometry

The geometry of the ejector will alter the flow field, which will, therefore, impact the mixing procedure. When the size is compact, this mostly results in a shift in background shock intensity. The background shock wave intensity plays a significant role when the ejector size is too small, limiting the mixing of the primary and secondary flows and leading to a higher pressure loss. When the size is too large, the performance of the ejector is slightly affected by the background shock wave. The major causes of the ejector's performance decline are the vortex loss brought on by the abrupt expansion effect and the adverse pressure gradient. The designs of each section of the system influence the ejector performance: the nozzle, mixing chamber, mixing duct, and diffuser section.

1.2.1.1 Nozzle Effect

The primary nozzle is a very critical component for the ejector-diffuser systems. It changes the characterization of the flow and system performance. The choking condition, flow velocity, and shock wave formation are related to the flow characteristics, and the nozzle's geometry is directly related to its geometry. For

example, the nozzle throat area is vital in controlling choking and shock wave formation. The nozzle throat area affects the formation and intensity of shock waves within the ejector system. In addition, a smaller throat area in the primary nozzle leads to higher fluid velocities, which increases momentum and enhances entrainment for improved suction performance. However, it is essential to avoid excessively high velocities as they can cause flow separation and losses. Therefore, the throat area should be designed carefully to achieve the desired velocity for efficient entrainment while mitigating adverse effects.

1.2.1.2 Mixing Chamber (Suction Chamber) Effect

The ejector system can be designed according to the position of the nozzle, which directly affects the mixing process. An ejector is called a "constant-area mixing ejector" when its nozzle's outlet is inside the constant-area region, and the mixing of the primary and entrained flows takes place inside the constant-area section. It can be seen in Figure 1-5. The ejector is known as a "constant-pressure mixing ejector" for the nozzle, with its exit positioned inside the suction chamber in front of the constant-area portion, as seen in Figure 1-6 [8]. The constant-pressure ejector, which is more extensively chosen, is known to operate better than the constant-area ejector [10].

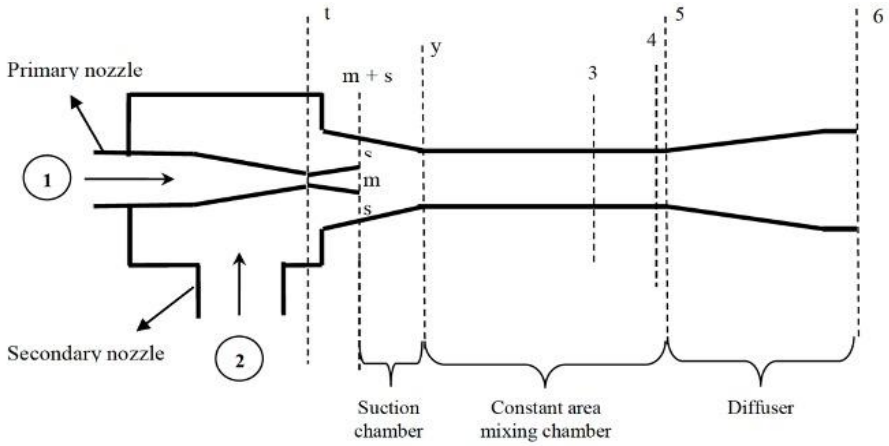

Figure 1-5 The constant pressure mixing ejector [10]

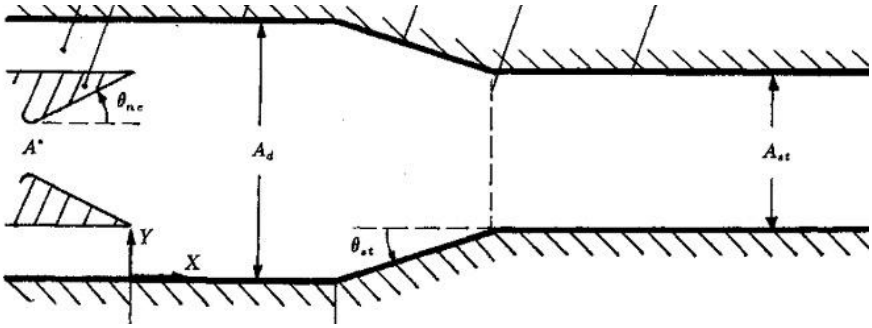

Figure 1-6 The constant area mixing ejector [11]

1.2.1.3 Mixing Duct and Diffuser Effect

For ejector design, the length of the mixing duct is significant, especially if the ejector structure has a narrow mixing zone. Momentum exchange between the primary and the secondary flow through mixing is the fundamental concept of the ejector. Because of this, the length of the mixing duct needs to be adequate to allow for effective mixing between the primary and secondary flows. A shock train is produced in the mixing duct, and the back pressure has an effect upstream in the mixing duct through the shock train. Because of this, the mixing duct must be long enough to include the shock train and enable the secondary flow area to be choked to achieve the critical mode in the ejector.

The diffuser of the ejector is positioned at the end of the system, and the kinetic energy of the mixed stream is converted to pressure energy. For enhanced pressure recovery, the outflow angle should be higher than zero [12]. The diffuser divergence angle is the diffuser's significant parameter. Two issues can be taken into consideration for the diffuser divergence angle. When this diverging angle is slight, the pressure drop increases due to friction. On the other hand, performance decreases for large diverging angles due to the boundary layer separation [13]. A well-designed diffuser geometry with gradual expansion, minimal flow separation, and controlled shock wave formation can significantly enhance the performance of an ejector-diffuser system by maximizing pressure recovery and minimizing losses.

1.2.2 Operating Conditions of System

The ejector performance can be influenced by different parameters, and the operating condition of the ejector is one of them. Pressure and temperature are the critical operating factors that change the shock and flow propagation inside the ejector. In this part, the effects of the primary and secondary flow's pressure and temperature on the performance are explained.

1.2.2.1 Pressure Effect

The primary flow complies with the principles of supersonic compressible flow. When the primary flow pressure rises, the mass flows through the primary nozzle, and the flow's momentum increases. The primary flow can under-expand even more and accelerate with a greater expansion angle because of the increase in momentum. As a result, the first oblique shock in the diamond flow pattern occurs at a higher Mach number. A jet core expands because of its larger expansion angle, which reduces the annulus effective area and the amount of secondary flow that can be entrained. Less suction on the secondary flow causes a decrease in ejector performance, but at the same time, higher momentum on the jet core changes shock wave position. The shock wave is observed to move downstream so the ejector can operate at a higher discharge pressure.

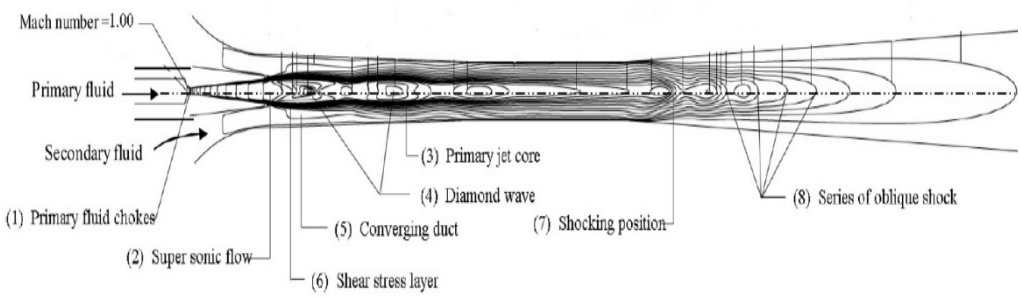

Figure 1-7 Mach number distribution along ejector [14]

A rise in secondary flow pressure impacts the expansion angle of an under-expanded wave. Reduced expansion angle due to pressure brings about a narrower jet core and

a higher effective area. At a lower Mach number, the expanding wave undergoes more acceleration. As a result, the jet core's momentum is decreased. Yet, a higher volume of secondary fluid could be entrained and forwarded through the converging duct due to an expanded effective area. The increased secondary fluid pressure recovers the jet core's reduction in the total momentum of the mixed stream [14].

1.2.2.2 Temperature Effect

Ejector operating modes affect variations of entrainment ratio with inlet temperatures. The density, speed of sound, and effective area at the throat alters the secondary mass-flow rate. When primary mass-flow rates rise, the effective area of secondary flow decreases. As a result, the secondary mass-flow rate increases slower than the primary mass-flow rate, and the entrainment ratio declines as the inlet temperature decreases. The entrainment ratio rises with reducing inlet temperature, and the growth rate of the secondary mass-flow rate is larger than that of the primary mass-flow rate [15].

1.3 Primary Flow Nozzle

A primary flow nozzle is an essential component of the ejector system, and it enables the entraining secondary flow by generating a low-pressure zone. The primary flow nozzle is specifically designed to accelerate the primary flow to high velocities and is usually positioned close to the ejector's inlet. As a result, the performance of the ejector could also be impacted by its design. The design considerations of the primary nozzle are nozzle exit position (NXP), throat diameter, and divergent and convergent section design.

It has been demonstrated in earlier research that the nozzle exit position (NXP), which is the distance between the primary nozzle exit and the entry of the constant area section, substantially affects the system's performance, especially the entrainment ratio. The change in NXP regulates the expansion angle and the region

inside the mixing section where the secondary flow can entrain. However, if the NXP is arranged too close to or too far from the mixing inlet, the mixed flow's momentum and compression are changed, affecting the entrainment ratio [16]. Different approaches explain the effects of the NXP, and it can be summarized that NXP is an empirical design parameter. There is no strict correlation that describes the relation between NXP and ejector performance. Optimization studies should be carried out to find the proper location for the primary nozzle and increase ejector performance.

The primary nozzle throat diameter influences the motive fluid's pressure and speed, which impacts the suction force generated at the nozzle exit. Higher suction forces and higher entrainment ratios occur from a larger nozzle throat diameter, allowing for a higher mass flow rate of the motive fluid. Nevertheless, a smaller nozzle throat diameter restricts the motive fluid's mass flow rate, reducing suction forces and entrainment ratios. Above a specific size, expanding the nozzle throat diameter could not, however, lead to further improvement in the entrainment ratio. Hence, there is no linear connection between the primary nozzle throat diameter and the entrainment ratio. To achieve the intended performance, the nozzle throat diameter must be optimized based on the unique design requirements and operating conditions of the ejector system.

The primary nozzle's structure is susceptible to how the divergent section is designed, especially when it is close to its optimal value. A tiny change might significantly impact how effectively the ejector works. Previous literature research studied the impact of the primary nozzle outlet diameter and divergent section length on the ejector under various entrained flow pressures. As stated in section 1.2.1.1, compared to the divergent section angle, the diverging section length only has a relatively little impact on the ejector performance. An optimized divergence angle is needed to maximize ejector performance by considering and comparing the entrainment ratios for different angles [17].

The primary nozzle structures influence entrainment performance at the critical and sub-critical modes of operation and the critical back pressure. There are various

designs for primary flow nozzles by considering the performance criteria. The choice of primary flow nozzle will depend on the ejector system's specific application requirements and expected performance characteristics. In general, converging or converging-diverging nozzles can be used in ejector system applications. However, for particular applications, such as mixing enhancement, there are additional designs. To increase mixing and suction inside the ejector system, there are artificial nozzle disturbers, chevrons, tabs, lobed mixers, corrugated surfaces, etc.

Tabs and chevrons are used to increase the mixing process and decrease the noise the jet produces, as shown in Figure 1-8 [18]. The tabs were investigated for mixing improvement in jets in the 1980s and 1990s. A tab is a flap positioned after the nozzle to alter the flow structure.

Figure 1-8 The left one is chevron nozzle and the right one is tabbed nozzle [18]

A chevron is a triangular vortex-forming device (vortex generator) whose inner surface is a smooth continuation of the inner surface of the nozzle exit. Because the form of flow interaction with the vortex generator depends on the exhaust regime (pressure ratio at the nozzle exit), these definitions apply to the vortex generator at the nozzle exit.

Lobed mixers/nozzles are fluid mechanic devices used to improve mixing in several applications. They are simply splitter plates with corrugated trailing edges, as shown in Figure 1-9. To lessen takeoff jet noise and fuel consumption, such devices have

been frequently used in turbofan engine exhausts and ejectors. Lobed mixers/nozzles have also become a popular option for boosting fuel and air mixing in combustion chambers to increase combustion efficiency and decrease the production of pollutants [19].

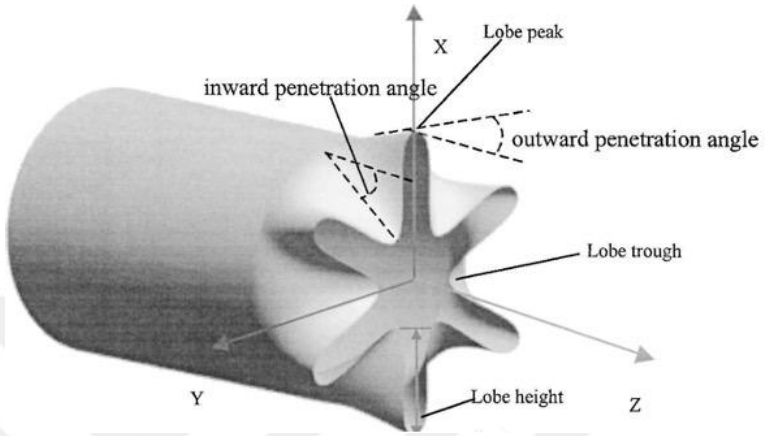

Figure 1-9 Lobed nozzle [19]

1.3.1 Chevron Nozzle

Chevron nozzles are a unique type of flow nozzles with a series of obliquely alternating vanes or teeth on their inside surface, as shown in Figure 1-10. As the fluid flows through the nozzle, chevrons cause it to swirl, creating vorticity in the shear layer and thus encouraging mixing and turbulence. The main difference between chevron and tab configuration is that chevron geometry causes more aggressive protrusion into the secondary flow.

In the shear layer of the potential core, chevrons on nozzles provide streamwise (axial) vorticity that enhances cross-stream transport and mixing. It has been noted that when the streamwise vorticity produced by the chevrons is tightly distributed, the vortices tend to swiftly eliminate one another, restricting the amount of cross-stream transport. The stronger axial vorticity accomplishes more transport and more mixing [20].

The chevron nozzle is a special kind of nozzle in terms of geometrical design. The parameters that affect the performance of the ejector system are the length of the nozzle, the inlet and exhaust diameter of the nozzle, the number of chevrons, the length of chevrons, and the penetration angle [21]. The geometric parameters of a simple triangular chevron nozzle are shown in Figure 1-10.

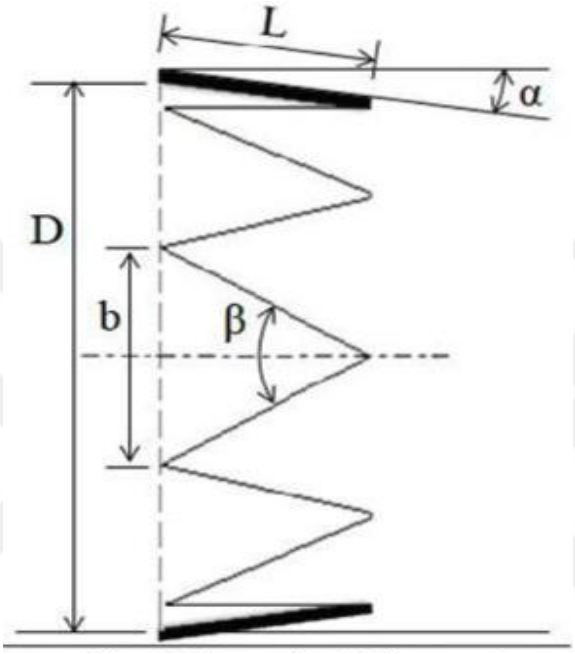

Figure 1-10 The geometric schema for chevron nozzle [21]

The base length of each chevron (b) can be calculated as,

$$b = \frac{\pi D}{N} \tag{1.3}$$

where D is the diameter of the nozzle and N is the number of chevrons

The chevron tip angle, β, can be expressed as

$$tan\ (\frac{\beta}{2}) = \frac{b}{2L} \tag{1.4}$$

By combining and rearranging these equations, it gives

$$(\frac{L}{D}) \times tan\ (\frac{\beta}{2}) \times N = \frac{\pi}{2} \tag{1.5}$$

The length of the nozzle, L, which is dependent on the exit diameter of the nozzle, D, is given as,

$$L' = 4.25 \times D \tag{1.6}$$

The height h of the chevron is

$$h = \frac{b}{2} \tag{1.7}$$

The equations demonstrate how the number of chevrons and tip angle affect the length of the chevron. These relationships imply that the main factors determining the geometry of the chevron are interrelated, making it impossible to change any one parameter without affecting the others.

The chevron penetration, chevron count, and chevron length characteristics of nozzle geometry are responsible for the distribution of the vorticity within the vortex core and influence the vortex's stability. Therefore, vortex intensity, vortex spacing, and vorticity distribution are the critical flow field characteristics, and they are controlled by the chevron characteristics [20].

The number of chevrons varies the spacing of streamwise (axial) vorticity. Increasing the chevrons generally leads to decreased spacing between the vortices formed in the flow. This is because more chevrons create more vortices, which tend to be closer together. The vortices produced by the chevrons can disrupt the flow and enhance mixing between the primary and secondary flows in the ejector.

Chevron penetration changes the strength of the streamwise vorticity and influences the potential core length. The increment in jet penetration leads to a decrement in the potential core length because of a critical rise in the streamwise circulation [22].

Chevron symmetry is also assumed as one of the design parameters. Chevron symmetry can influence flow control, noise reduction, and pressure recovery in ejectors. Symmetrical chevrons can help control the boundary layer's behavior by promoting more uniform flow patterns and preventing boundary layer separation. This allows for better control over the flow dynamics and minimizes disturbances.

The chevron length relates to the vorticity distribution within the streamwise vortices. To understand the concept of vorticity distribution, the streamwise vortices should be analyzed in detail. These vortices are believed to have a "calming effect," which lowers total shear layer turbulence. With the baseline nozzles, the angular component contributes to most of the vorticity in the shear layer. These unique helical coherent structures are where the vorticity of this process focuses. As they spread downstream, these structures experience interactions and slowly evolve. Their chaotic and active dynamics result in high turbulence intensities [23].

More longitudinal vortices were produced, and the nozzle encompassed a more secondary stream into the ejector under the impact of the chevrons. More energy would transfer between both flows because of improved mixing. As a result, in contrast to the model with the convergent nozzle, the shock wave turned into a weak wave. More flows would be entrained, and more energy would be saved [24].

1.4 Mixing Phenomena

In engineering applications, mixing improvement has an important role, especially in aircraft engines. There are numerous different techniques to study the supersonic turbulent mixing process. The mixing process has been evaluated and quantified using a variety of concepts, including the spread rates of jets, the degradation of potential cores, and others [25].

It is identified that the supersonic primary stream exits the primary nozzle with a Mach number that is higher than one. As a result, it can extend and accelerate through a diffuser. Depending on the Mach number, it can be called an under-expanded or over-expanded. The first sequence of oblique shock and expansion waves, often known as the "diamond wave" pattern, is intended to maintain static pressure between the primary jet core and the surrounding fluid over the free boundary. The variation in static pressure at the ejector's center line as the flow proceeds through a mixing chamber can be used to study this phenomenon [14].

A diamond wave jet core in the mixing chamber implies a semi-separation between the surrounding secondary fluid and the high-speed primary flow. Hence, the convergent duct sucks a second fluid into the mixing chamber. Further, the shear stress layer interacting between these two streams is illustrated by the noticeable velocity distinction between them. After the secondary fluid is entrained and enters contact with the expanding wave, shear mixing of the two streams occurs. The secondary fluid accelerates through the converging duct because of the shear mixing process; on the other hand, the diamond wave descends because of the shear mixing and fluid viscosity. During the initiation of the flow process, the static pressure of the flow progressively declines, and the intensity of the diamond wave diminishes [14].

Several researchers have proposed the use of vorticity to improve supersonic mixing. The streamwise and spanwise are two main types of vortices that will be studied in this part to investigate the mixing process in the flow field.

The streamwise vortices are a component of the steady flow characteristic. They are more durable over a wider area and do not exhibit as active dynamics as angular structures. Be aware that the boundary layer of the nozzle is the only source of vorticity in the flow. At the expense of the angular component, the chevrons relocate some of it into the streamwise piece. Consequently, by forming streamwise vortices, the chevrons partially restrain the energetic activity of the angular coherent structures [23]. The vortex component orthogonal to the streamwise vortices is known as the spanwise (longitudinal) vortices. The velocity differential between the primary flow and the secondary flow at the edge of the geometric structure causes the spanwise vortices, which are generated by viscous shear forces. The streamwise vortices and the spanwise vortices interact as the fluid flow develops. The largest velocity difference between the primary flow and the secondary flow occurs at the beginning of the mixing process, and most of the vortex structure close to the nozzle comprises spanwise vortices. The spanwise vortices at the nozzle outlet extend toward the wall as fluid flow develops and progressively diminishes [26]. Equations (1.8) and (1.9)

define the two types of vortices named as streamwise vortices and spanwise vortices respectively.

$$\Omega_s = \Omega_x = (\frac{\partial w}{\partial y} - \frac{\partial v}{\partial z}) \tag{1.8}$$

$$\Omega_n = \sqrt{{\Omega_y}^2 + {\Omega_z}^2} = \frac{D}{U_0}\sqrt{(\frac{\partial u}{\partial z} - \frac{\partial w}{\partial x})^2 + (\frac{\partial v}{\partial x} - \frac{\partial u}{\partial y})^2} \tag{1.9}$$

1.5 Objectives and Outline of the Thesis

Ejector systems operate as vacuum systems in this thesis study. Despite their seemingly straightforward nature, these systems comprise flow processes, including supersonic conditions, shock wave generation, turbulent mixing, and multiple shock systems.

The objective of this study is to investigate the impact of a primary flow nozzle, specifically the Chevron nozzle, on the mixing process. In contrast to conventional nozzles, the Chevron nozzle is selected to analyze its effect on the mixing process and the performance of the ejector-diffuser system. To achieve this goal, a numerical methodology is developed to assess the Chevron nozzle and compare its results with those of a conventional nozzle. The numerical findings are subsequently validated through investigations utilizing the TÜBİTAK SAGE's experimental setup.

During the experimental phase, a fabricated Chevron nozzle is subjected to various configurations and operational conditions. Pressure transducers measure test data from distinct points within the ejector-diffuser setup. These test results are then compared with the circular nozzle results to determine the increase in ejector performance. Ultimately, the Chevron nozzle's impact on mixing process efficiency and its potential applications within ejector systems are thoroughly examined.

CHAPTER 2

LITERATURE REVIEW

In this chapter, the previous studies related to the topic are mainly explained. In this field, primary flow nozzle studies are developed by considering the performance of the ejector-diffuser system. The previous works related to primary flow nozzle are presented in two sections: numerical studies and experimental studies.

2.1 Numerical Studies

Jin et al. worked on the implicit finite volume solution using the Reynold stress model. This method was applied to a three-dimensional chevron nozzle in an ejector-diffuser system, and the performance effects were studied. In this study, the results of the chevron were compared with a conventional convergent nozzle, shown in Figure 2-1. This problem of the study was solved both numerically and by using a one-dimensional mathematical model. The results showed that the configuration of the primary jet intensely influenced dynamic conditions. At the end of the solution, the unsteady behavior of the recirculation zone reached an equilibrium state, and it was observed that the chevron accelerated the transient flow and increased the entrained stream [27].

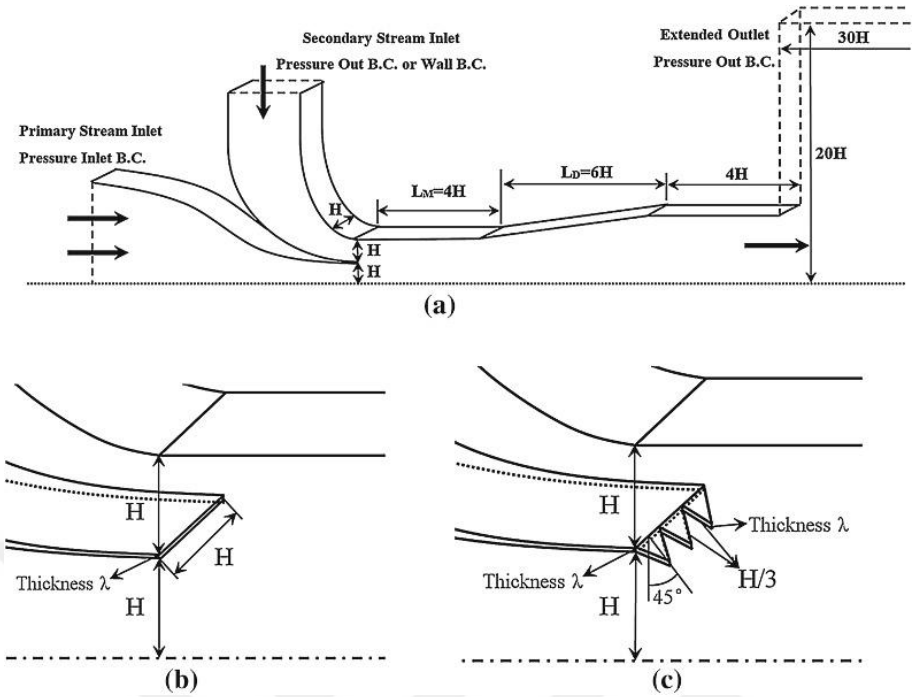

Figure 2-1 Three-dimensional chevron nozzle model [27]

The performance of supersonic ejectors can be analyzed with different numerical techniques. In the study of Macia et al. [28], vacuum generation was solved explicitly and implicitly. High Speed Aerodynamic (HiSA) solver was used as an implicit solver, and rhoCentralFoam (RCF), an unsteady density-based compressible solver of the OpenFoam platform, was used as an explicit solver. Two solvers reached a good agreement. Also, two regimes were observed during the solution, which were the supercritical and subcritical regimes.

To design the primary flow nozzle, an optimization process is inevitable. Wang et al. [17] worked on the numerical optimization of some design parameters to improve ejector performance, including convergent and divergent sections' geometry, surface roughness, and primary flow nozzle length. In this study, steady-state flow was assumed inside the adiabatic inner walls. The simulation findings revealed that during the design of an ejector, more focus should be given to the throat and diverging part of the primary nozzle since their length and surface roughness significantly impacted the ejector's entrainment ratio.

Fu et al. investigated the influence of two design parameters, primary nozzle outlet diameter and divergent section, on the ejector performance. The results of this study results showed that the length of the divergent section had comparatively less influence [29]. The entrainment ratio increased with the length of the diverging section, reached a maximum, and started to decrease. After some empirical calculations, divergent section length was decided. Also, nozzle outlet diameter was an empirical parameter according to this study. There was an optimum range for outlet diameter to get the best performance from the ejector.

Yadav et al. [16] focused on the lengths of different sections and the position of the primary nozzle. In this study, the variation in the performance of an ejector was analyzed by changing the lengths of the mixing and diffuser sections. In addition, the nozzle exit was positioned at seven different points, and its effect was investigated. According to entrainment ratio variation, optimum nozzle exit position and diffuser section lengths were determined.

In the study of Li et al., the impact of the nozzle throat and exit diameters on the ejector performance was investigated. The CFD method was applied to two-dimensional steam ejectors with different geometries, and the critical performance curves of ejectors were obtained. Their results claimed that the nozzle throat diameter critically impacted the flow structure [1].

The nozzle exit position (NXP) is another design parameter that affects the ejector system's performance. As it is explained in section 1.3, NXP changes the flow structure. Rand et al. investigated a single-phase ejector to get more details about the nozzle exit position (NXP). They found that the NXP affects the location of the critical pressure location, and as a result, the entertainment ratio was varied [30]. The optimization was applied to the different values of NXP, and finally, the performance of the ejector was maximized.

Ejectors are not high-performance systems; thus, enhancement is compulsory for them. In the literature, there are different approaches to increase their performance. Xue et al. wanted to investigate the impact of using different kinds of primary

nozzles on performance. They selected three different geometric tips: conical, petalage, and crenation [31].

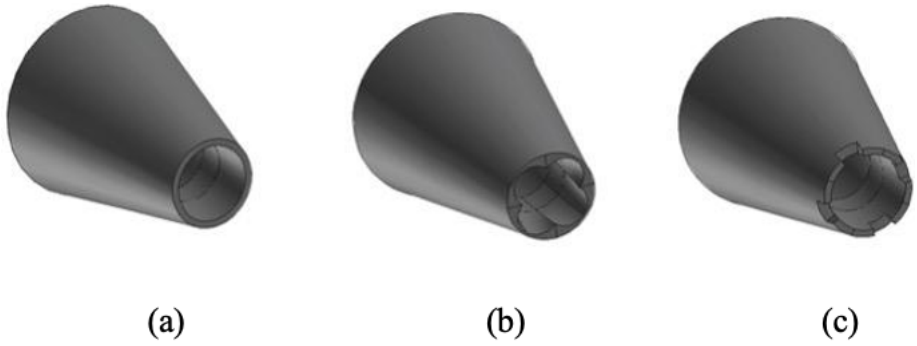

Figure 2-2 (a) Conical nozzle, (b) petalage nozzle and (c) crenation nozzle [31]

The three different nozzle types were compared according to their entrainment ratio and vacuum capacity. It was seen that the crenation nozzle had the highest entrainment ratio, and the conical nozzle had higher entrainment than the petalage nozzle.

Chevron nozzle is preferred for enhanced mixing needed in the system. The nozzle with chevrons is commonly used in aerospace studies and aviation engines. It has various benefits, including improving the performance of conventional converging-diverging nozzles or convergent nozzles and reducing jet noise and infrared signatures. Kong et al. used a chevron nozzle instead of a conventional convergent nozzle in their ejector-diffuser study. They compared the effect of chevrons on performance improvement in terms of the entrainment ratio, pressure loss, and pressure recovery [32]. Three different nozzles, the convergent nozzle, the new nozzle design with six chevrons, and the new nozzle design with ten chevrons, were solved numerically using a commercial flow solver, ANSYS Fluent.

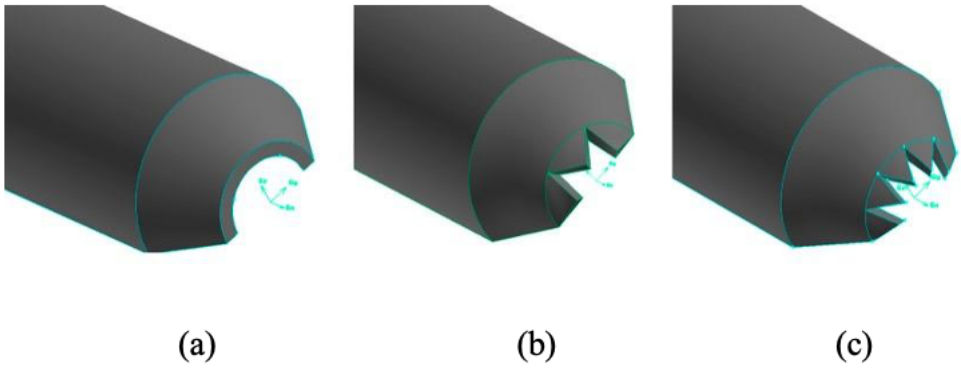

Figure 2-3 (a) Convergent nozzle, (b) new nozzle design (6 chevrons), (c) New designed nozzle (10 Chevron) [32]

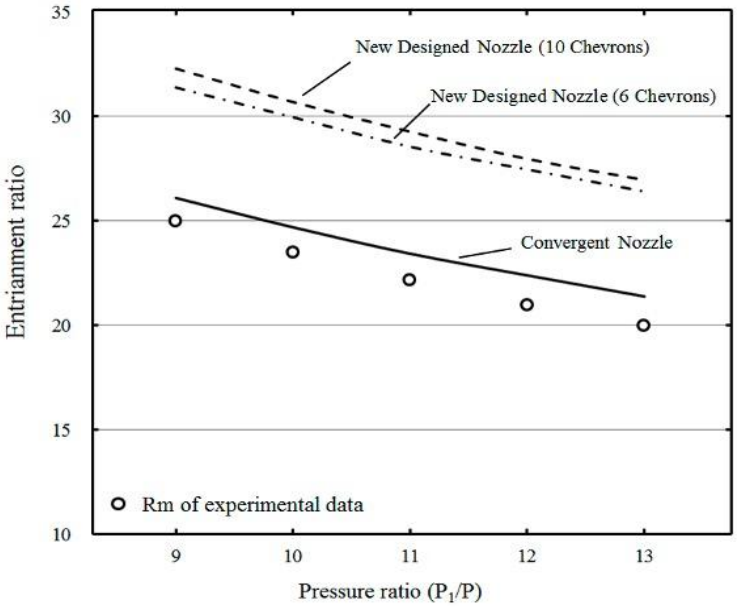

Figure 2-4 Pressure ratio versus entrainment ratio graph [32]

The results show that better performance was observed in ejectors having nozzle with ten chevrons. The pressure recovery was improved by 8.5%, and entrainment ratio was increased by 14.8%.

One of the aims of using chevrons in the nozzle design is its turbulence effect, and to investigate the turbulent characteristics, there are plenty of studies. Kotian et al. studied the turbulent characteristics of a compressible jet computationally [33]. Using a chevron nozzle with a chevron crest angle of 450, the turbulence

characteristics of the flow were examined. The results showed that the mixing of two streams was enhanced due to the formation of a counter-rotating pair of vortices close to the chevron nozzle exit.

Chevron nozzles are used in different kinds of systems. Although they are commonly preferred in aerospace applications, they can be also used in refrigeration systems. Kim et al. had a study about the transient flow through the chevron nozzle in a refrigeration system. To model the equilibrium flow characteristics, the transient numerical method was applied in the secondary chamber. The results showed that the starting time was decreased at a lower equilibrium pressure when a chevron nozzle was used instead of a convergent nozzle [34]. The reason behind these results was explained by more longitudinal vortices and more rotational stream produced in the mixing chamber due to the presence of chevrons. As a result, the performance of the vacuum ejector-diffuser system was greatly boosted, and the mixing process was improved.

2.2 Experimental Studies

In this part, the experimental studies are illuminated in detail. As explained before, mixing enhancement is crucial in improving ejector performance. For this purpose, there were different approaches and studies in the literature. Some were related to the design, while others prioritized operating conditions, but the common issue was generating vortices to enhance the mixing between flows. There are different types of nozzles to create more swirls in flow, like chevron, lobe, or tab. In addition to them, some devices are specifically designed for these purposes.

In the Penn State Supersonic Wind Tunnel, Naughton et al. studied vortex and vortex/shock interaction [25]. They used a strut-mounted swirl injector to create streamwise vorticity. In the experimental setup, Laser Light Sheet (LLS) images were utilized to validate mixing phenomena. The test setup is shown in Figure 2-5.

The results showed that the mixing process was enhanced by 34% because of the rise in streamwise vortices.

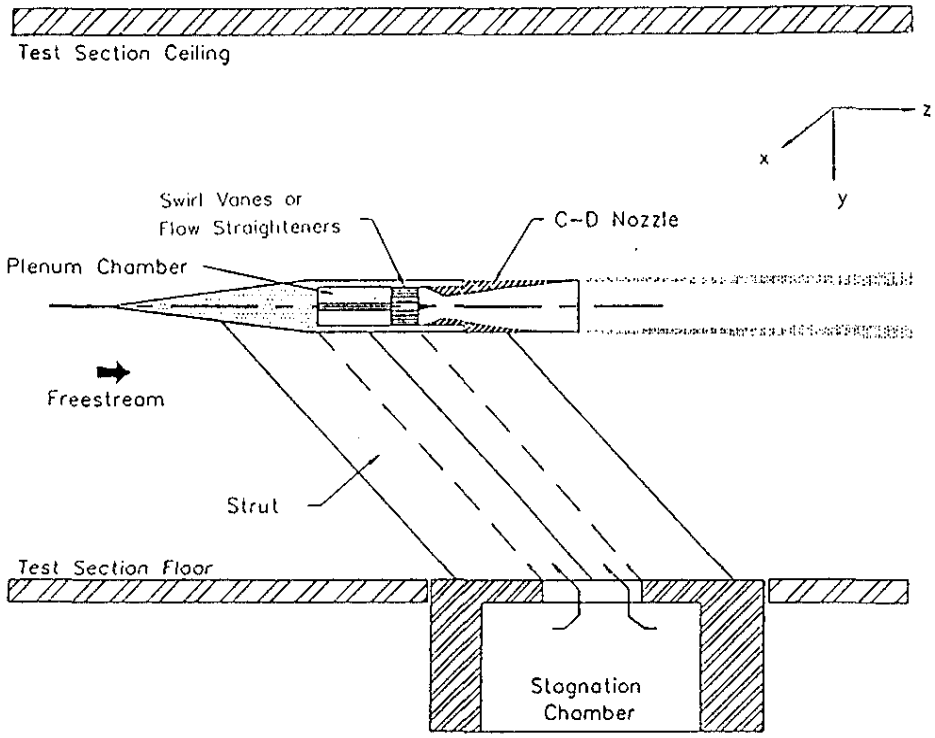

Figure 2-5 Vortex generator setup [25]

Subramanian et al. [22] studied the effect of the design of a chevron and the impact of using a chevron nozzle instead of a convergent nozzle, as shown in Figure 2-6a and Figure 2-6b. This study validated the mixing enhancement due to the chevrons. Improvised tabbed chevron nozzle in Figure 2-6c was tested, and the results showed that due to geometry modification, the spreading rate of the jets was accelerated, and the mixing rate was increased.

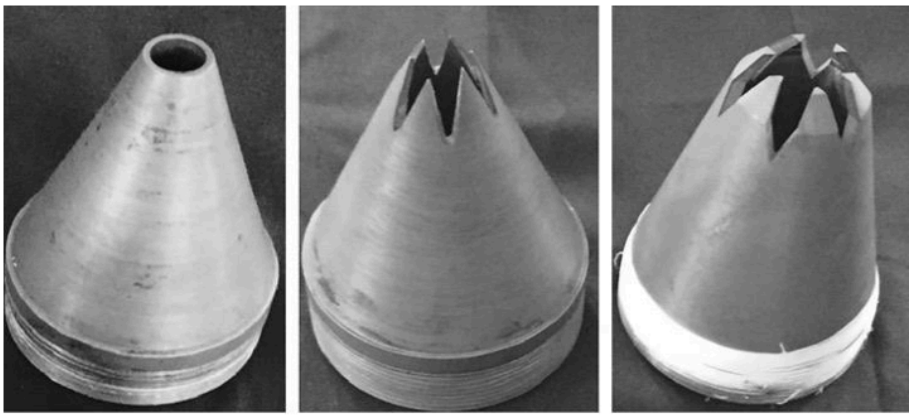

(a) (b) (c)

Figure 2-6 (a) Convergent nozzle, (b) Chevron nozzle, (c) Improvised tabbed chevron nozzle [22]

Callender et al. carried out a study about serrated (chevron) nozzles. This experimental study measured the chevron impact on the mean and turbulence field using Particle Image Velocimetry PIV. Two different test setups were used. The first setup measured axial and radial velocity components in a two-dimensional plane parallel to the axial component [35]. In the second setup, another plane was positioned perpendicular to the axial component of the jet, and stereoscopic images were taken from the test setup. In the results, turbulent kinetic energy (TKE) was increased near the center of the nozzle lip because of the interaction of the secondary jet with the slower outer stream.

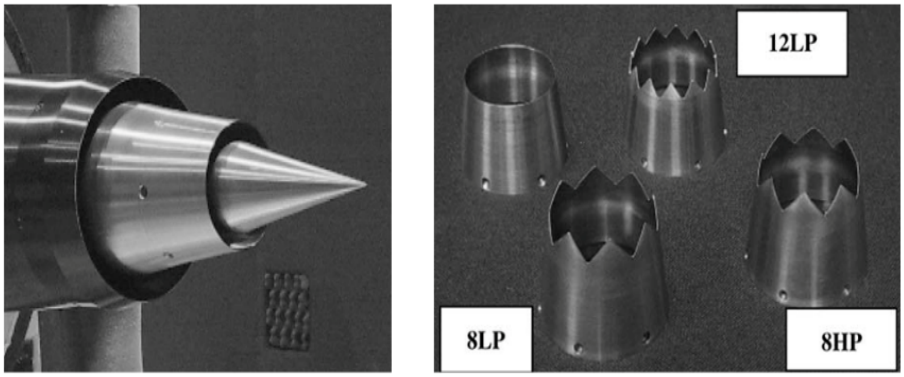

Figure 2-7 Serrated (chevron) nozzle types [35]

Bridges and Brown carried out a parametric testing study to understand the effects of chevron parameters [20]. For that purpose, they worked on ten different chevron nozzle configurations. Chevron count, length, symmetry, and penetration parameters were varied and tested.

As explained in Bridges and Brown's study, the chevron nozzle has an acoustic impact. In aerospace applications, acoustic is one of the critical problems, and there are studies related to noise reduction. In supersonic flow, noise reduction is a complicated problem, and researchers found that a chevron nozzle positively affects acoustic difficulties. Tide and Srinivasan made acoustic measurements over various nozzle pressure ratios from sub-critical to under expansion phases, acoustic measurements such as overall sound pressure level, spectra, directivity, acoustic power, and broadband shock noise [36].

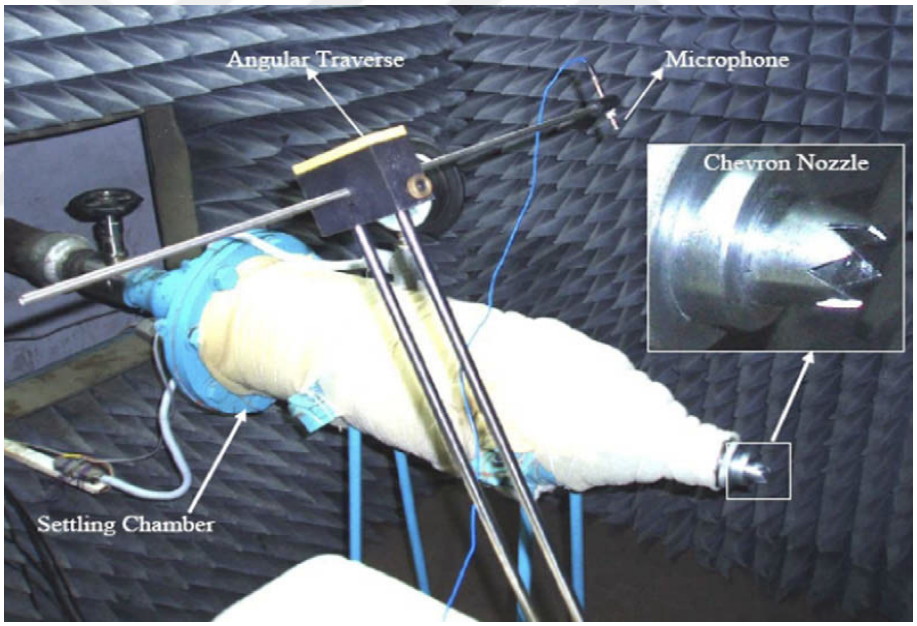

Figure 2-8 Test set-up of chevron nozzle testing for acoustic [36]

They found that a higher chevron count and a smaller penetration for low and medium nozzle pressure ratios produce the maximum noise suppression. The chevron nozzle with eight lobes and a 0° penetration angle provided the greatest noise reduction of all the examined geometries. The performance of the various

chevron nozzles had been objectively assessed using the acoustic power index. Tide and Srinivasan claimed that chevron count was the essential noise reduction criterion at low nozzle pressure ratios, but chevron penetration was critical at high nozzle pressure ratios.

As the literature shows, the ejector-diffuser system is a broad concept in industrial applications with numerous parameters to explore. On the other hand, the chevron nozzle is a distinct type used for specific purposes due to its intricate geometry. In this thesis study, different chevron nozzle design from literature studies is applied to an ejector-diffuser system, and critical parameters are varied to observe their effects on performance. The chevron effect and design parameters are examined numerically and experimentally, which has yet to be studied in the literature. This thesis study is believed to shed light on the mysteries surrounding the chevron concept and is expected to serve as a reference model for future studies.

CHAPTER 3

NUMERICAL METHODOLOGY

3.1 Introduction

In this chapter, the numerical methodology for ejector study is explained. Numerical methodology contains CAD model, Fluent solver details and Grid Analysis. The numerical study is achieved using the commerical ANSYS Fluent 19.2 software. At the end of the chapter, details about previous research on ejector systems are given.

3.2 CAD Model

- Ejector System Geometry

In this section, the three-dimensional CAD model of the ejector system is represented in Figure 3-1, and the internal flow model is illustrated in Figure 3-2. CFD analyses are performed by using this flow model.

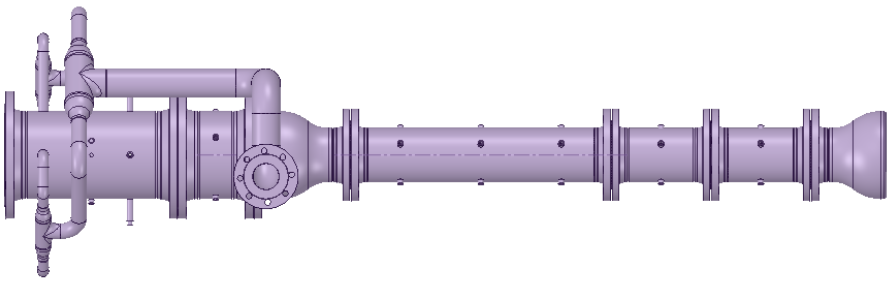

Figure 3-1 CAD Model of Ejector-Diffuser

The basic dimensions are described in the model: lengths and diameters. L1 is the length of the ejector-diffuser system and 2422 mm. L2 is the length of the mixing duct section and 1487 mm. In addition, D1 is the diameter of the spool section and 263 mm. Also, D2 is the mixing duct section and 158 mm.

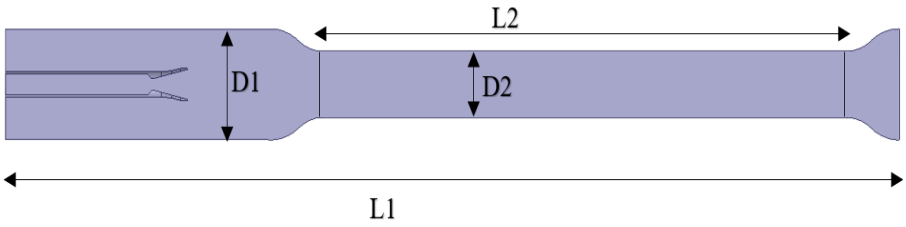

Figure 3-2 Internal Flow Model of Ejector-Diffuser

Table 3-1 Dimensions

Geometric Parameters	(mm)
Length of the ejector-diffuser, L1	2422
Length of the mixing duct, L2	1560
Diameter of the spool, D1	263
Diameter of the mixing duct, D2	158

- Chevron Nozzle Geometry

A Chevron nozzle is a special kind of nozzle with more design parameters than conventional nozzles. In this study, the length and width of the chevron and the penetration angle are used as geometric parameters. The length and width of the chevron are 20 mm and 13.8 mm, respectively. Moreover, the penetration angle is 5.1 mm.

3.3 The CFD Solver

3.3.1 Governing Equations

In numerical study, CFD analysis is performed to solve flow equations. During calculation, the fundamental fluid dynamics laws are solved. These are conservation of mass, momentum, and energy law. In this study, three-dimensional calculations are performed using the basic five unknown parameters. Pressure, temperature, density, velocity, density, and internal energy are described as unknown parameters

in governing equations. Air is used as a working fluid, which is assumed to be the ideal gas form. Thus, ideal gas law is applied to the system primarily. This law implies that pressure is defined by density, temperature, and specific gas constant.

$$P = \rho RT \tag{3.1}$$

$$R = \frac{R_u}{M} \tag{3.2}$$

In this formula, R_u represents the universal gas constant, and it equals 8314.4621 J/mol.K. M represents the molecular weight of the gas, and M equals 28.97 g/mol for air. Thus, the specific gas constant is calculated as 287.1 J/kg. K for air. Another unknown parameter of internal energy can be calculated with a function of temperature by using the ideal gas law.

$$e = c_v T \tag{3.3}$$

The fundamental fluid dynamics equations are calculated by the following equation. The thermal conductivity, k, and the viscosity, μ are asssumed in this study.

The conservation form of mass

$$\frac{\partial(\rho u)}{\partial t} + \nabla.\left(\rho u\vec{V}\right) \tag{3.4}$$

The conservation of momentum

$$\frac{\partial(\rho u)}{\partial t} + \nabla.\left(\rho u\vec{V}\right) = -\frac{\partial p}{\partial x} + \frac{\partial \tau_{xx}}{\partial x} + \frac{\partial \tau_{yx}}{\partial y} + \frac{\partial \tau_{zx}}{\partial z} \tag{3.5}$$

$$\frac{\partial(\rho v)}{\partial t} + \nabla.\left(\rho v\vec{V}\right) = -\frac{\partial p}{\partial y} + \frac{\partial \tau_{xy}}{\partial x} + \frac{\partial \tau_{yy}}{\partial y} + \frac{\partial \tau_{zy}}{\partial z} \tag{3.6}$$

$$\frac{\partial(\rho w)}{\partial t} + \nabla.\left(\rho w\vec{V}\right) = -\frac{\partial p}{\partial z} + \frac{\partial \tau_{xz}}{\partial x} + \frac{\partial \tau_{yz}}{\partial y} + \frac{\partial \tau_{zz}}{\partial z} \tag{3.7}$$

The conservation of energy

$$\frac{\partial(\rho e)}{\partial t} + \nabla.\left(\rho e\vec{V}\right) = \rho\dot{q} + \frac{\partial}{\partial x}\left(k\frac{\partial T}{\partial x}\right) + \frac{\partial}{\partial y}\left(k\frac{\partial T}{\partial y}\right) + \frac{\partial}{\partial z}\left(k\frac{\partial T}{\partial z}\right)$$

$$-p\left(\frac{\partial u}{\partial x}+\frac{\partial v}{\partial y}+\frac{\partial w}{\partial z}\right)+\lambda\left(\frac{\partial u}{\partial x}+\frac{\partial v}{\partial y}+\frac{\partial w}{\partial z}\right)^2$$

$$+\mu\left[\begin{array}{c}2\left(\frac{\partial u}{\partial x}\right)^2+2\left(\frac{\partial v}{\partial y}\right)^2+2\left(\frac{\partial w}{\partial z}\right)^2+\left(\frac{\partial u}{\partial y}+\frac{\partial v}{\partial x}\right)^2\\+\left(\frac{\partial u}{\partial z}+\frac{\partial w}{\partial x}\right)^2+\left(\frac{\partial v}{\partial z}+\frac{\partial w}{\partial y}\right)^2\end{array}\right] \quad (3.8)$$

3.3.2 Turbulence Models

Turbulence is a complicated phenomenon that appears in a variety of applications. One of the most crucial elements of CFD modeling is turbulence modeling, and accurately modeling turbulence is essential to getting precise CFD results. There are types of turbulence models according to the governing equations and numerical approach used to compute turbulent viscosity. The most common approaches are Reynolds-averaged Navier-Stokes equations (RANS), Large Eddy Simulation equations (LES), and Direct Numerical Simulation (DNS). DNS and LES approaches provide higher degrees of freedom, but their computational costs are much higher than the RANS approach. DNS and LES approaches are generally preferred in simpler geometries and for academic purposes. RANS is commonly used in complex geometries in industrial applications. The main two-equation models are k-ε, k-ω, and SST k-ω.

3.3.2.1 k-ε Turbulence Model

Turbulent kinetic energy and dissipation equation models are used in the solution. The k-ε model uses the epsilon equation for the turbulent energy dissipation rate.

- The parameter epsilon determines the distinctive linear turbulence scale, while the parameter k determines the turbulence energy.

- The near-wall flows, particularly those with large pressure gradients, are not accurately described by this model. It gives a better solution for being far away from the wall.
- It is a suitable method for external flow interactions but not a good option for jet flows or robust curvature into a flow.

3.3.2.2 k-ω Turbulence Model

Turbulent kinetic energy and dissipation equation models are used in the solution. In contrast to the k-ε model, the k-ω model uses the omega equation for the turbulent energy dissipation rate.

- The parameter ω determines the distinctive linear turbulence scale, while the parameter k determines the turbulence energy.
- The near-wall flows, particularly those with large pressure gradients, are accurately described by this model.
- However, it is not an excellent option to calculate jet streams.

3.3.2.3 SST k-ω Turbulence Model

Turbulent kinetic energy and dissipation equation models are used in the solution. In this model, two models are combined. For near the wall region, k-ω model is used, and far away from the wall region, k-ε model is used.

- This model is beneficial in mixing layers' problems at medium-pressure gradients.
- Separated and jet flows can be solved by using SST k-ω model, but it is difficult to converge the solution.

As mentioned before, turbulence is calculated using the commercial Fluent tool. Fluent provides RANS methods for the numerical scheme. The proper model is selected concerning the solution domain and the flow characteristic. In this study,

the mixing of two streams is a critical issue. In the literature, for the ejector system with a chevron nozzle and the mixing problems, SST k-ω was used. Therefore, the SST k-ω model was applied for turbulence calculation.

3.4 FLUENT Setup

In this thesis study, ANSYS Fluent is used for CFD solution, and the proper setup conditions are selected for ejector flows. Due to the compressible flows of the ejector, the computations are performed using a density-based type solver. In addition, the calculations are performed in steady state condition.

- Air is used for both primary nozzle flow and secondary flow. Air is accepted as compressible, and ideal gas equations are applied during the solution process. Also, Sutherland is taken as a viscosity function for air.

- The RANS method is used as a viscous model. For turbulence solution, the SST k-omega model is applied.

- The boundary conditions are arranged according to flow-inlet and flow-outlet boundaries. The primary flow and secondary flow inlets are defined as pressure inlets. The outlet of the ejector system is defined as a pressure outlet. Three-dimensional solid geometry is solved in half of its size, and half plane is defined as symmetry boundary condition. The rest of the geometry boundaries are defined as wall boundary conditions.

Figure 3-3 Boundary definitions of ejector system

- The spatial discretization method is second order upwind for pressure, momentum, turbulent kinetic energy, and turbulent dissipation rate.

Table 3-2 Fluent Setup Details

Solver Type	Density Based Solver
Time Dependency	Steady State
Phase Type	Single Phase
Turbulent Model	SST k-omega
Pressure Discretization	Second Order
Momentum Discretization	Second Order Upwind
Turbulent Kinetic Energy Rate Discretization	Second Order Upwind
Specific Dissipation Rate Discretization	Second Order Upwind
Energy Discretization	Second Order Upwind

3.5 Grid Sensitivity

Numerical simulation is relatively easy but requires highly qualified program handling, input variable accuracy, and grid or mesh optimization skills. A high-quality grid produces great order accuracy while reducing errors and maintaining a fair calculation time. In general, using fine grids produced highly precise results, but the computational duration takes longer. As a result, it is necessary to test the grid's sensitivity appropriately.

In this thesis study, a grid sensitivity analysis is implemented using three different grid size options, which are fine, medium, and coarse mesh. Firstly, the coarse mesh is used, and the total mesh number is 150000. The pressure and mass flow rate results are saved for comparison. Secondly, the medium mesh is used, and the total mesh number is 609921. In this case, the pressure and mass flow rate results are also saved for comparison. Finally, fine mesh is used; the total mesh number is 2190182. The results are tabulated in Table 3-3.

Table 3-3 Grid Analysis Results

Mesh Size	Mesh Element Number	Primary Inlet Mass Flow Rate (kg/s)	Secondary Inlet Mass Flow Rate (kg/s)	Primary Flow Pressure (kPa)	Secondary Flow Pressure (kPa)
Coarse Mesh	150000	1.4216	0.542	1952.5	29.35
Medium Mesh	609921	1.424	0.551	1952.3	29.33
Fine Mesh	2190182	1.424	0.551	1952.3	29.33

Grid analysis is performed with the same boundary conditions and different mesh element sizes. The results in Table 3-2 prove that decreasing mesh sizes and increasing mesh element numbers do not create a big difference between solutions after some point. The difference between medium and fine mesh is at a decimal level. To get a more accurate result, 2 million polyhexcore mesh is used for flow analysis. However, it can be affirmed that after 2 million mesh element numbers, the results will stay the same, and much higher computational effort will be needed.

In addition to the number of mesh sensitivity, different meshing methods are applied to the design. The chevron nozzle is a unique geometry requiring finding the appropriate mesh structure. Three different mesh methods are used: tetrahedron mesh, hex mesh, and polyhexcore mesh, and the result accuracy is compared. The results show that polyhexcore, which Fluent Meshing creates, generates a good quality solution for this geometrical problem.

3.6 The Previous Ejector Study

The primary purpose of this study is to observe the chevron effect on vacuum capability. Chevron nozzle results are compared with the previous ejector study, which contains a circular nozzle to achieve this purpose. This study was performed in TÜBİTAK SAGE in 2021 with the same experimental setup, and the focus of this

study is on the test section of the High-Altitude Test System. To investigate the chevron effect, this study's results for the test chamber section are beneficial. The system geometry and its size are the same for both cases. The Fluent setup also selected the same options.

In that study, three different free jet mass flow rates were examined in two different Mach numbers, 2 and 2.5. It was observed that the error between CFD results, and test results is much lower when the Mach number is two, and thus, Mach number 2 results are selected to compare the test results shown in Table 3-4.

Table 3-4 The Reference Study Results

Test Number	Mach Number	Free-Jet Nozzle Mass Flow Rate (g/s)	Free-Jet Nozzle Inlet Pressure (Pa)	Test Chamber Static Pressure (Pa)
Test-1	2	750	115500	3800
Test-2	2	1300	178500	5900
Test-3	2	1500	206000	6800

In these results, the critical parameter is the test chamber's static pressure because this study aims to observe the chevron's vacuum effect. It is expected that the chevron nozzle can draw a higher volume of air. Accordingly, the test chamber should maintain a lower pressure level due to the decreased mass flow rate. Therefore, "Test Chamber Static Pressure" is the comparison parameter between the two studies.

CHAPTER 4

EXPERIMENTAL STUDY

4.1 Introduction

In this section, an experimental study is explained, which is utilized to validate the numerical study. The experimental study is performed in TÜBİTAK SAGE Test Setup (TAYFUN). Firstly, the test setup and its details are explained. Then, The experimental matrix is represented. Test conditions are varied concerning the spool component and the length of the mixing duct. The details are illuminated in Section 4.4.

4.2 Experimental Setup

The TÜBİTAK SAGE HAT test setup integrates two sections: the ejector system and the test section. In this thesis study, the significant part is the ejector-diffuser section. However, pressure and temperature data are measured from the test chamber in the test section for comparison. In Figure 4-1, the two-dimensional sketch is shown.

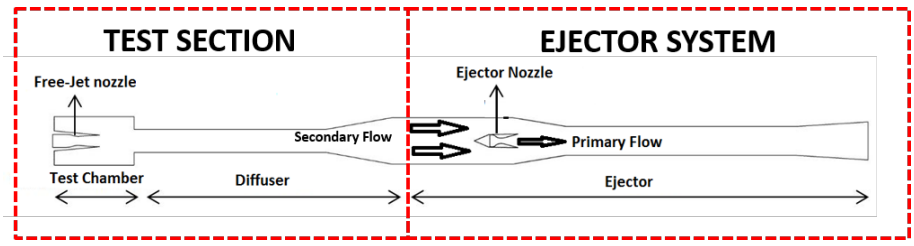

Figure 4-1 Two-dimensional sketch experimental setup [2]

Different parts are connected in the system using flanges, and the experimental setup is shown in Figure 4-2.

Figure 4-2 Experiment Setup

Table 4-1 Component Names of Setup

Number	Component Name
1	Free Jet Feed Line
2	Test Chamber
3	Test Chamber Diffuser
4	Ejector Nozzle Feed Line and Manifold
5	Spool
6	Ejector-Diffuser
7	Subsonic Diffuser

4.2.1 Free Jet Nozzle Feed Line Component

The free jet nozzle feed line is connected to the test chamber part, and it is the starting component for the flow through the secondary flow inlet of the ejector system. It supplies the defined mass flow rate through the test chamber section.

4.2.2 Test Chamber Component

Test items are generally positioned inside the test chamber of the test setup, and four-point measurement devices are integrated to pressure and temperature data. In this study, the inside of the test chamber is empty, but pressure and temperature test data are taken from the pressure transmitter and thermocouple at the top of the test chamber.

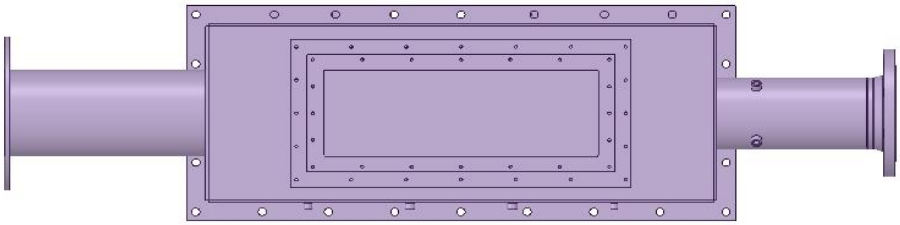

Figure 4-3 CAD model of test chamber

Figure 4-4 Test chamber in experimental setup

4.2.3 Test Chamber Diffuser Component

The test chamber diffuser is positioned between the test chamber and ejector-diffuser sections. After the free jet flow exits the test chamber, it enters this part and is expanded into the ejector diffuser system as a secondary flow. The pressure data are also measured from the top of this section.

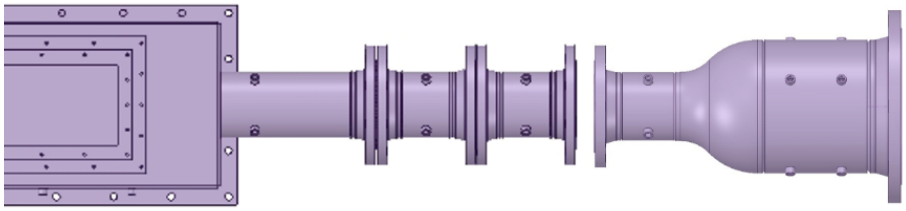

Figure 4-5 CAD model of test chamber diffuser

Figure 4-6 Test chamber diffuser in setup

4.2.4 Ejector Nozzle Feed Line and Manifold Component

The ejector nozzle feed line and manifold section is built with 4 piping elements and its directly mounted to the primary nozzle inlet around. The high pressure is transmitted with a feed line and spread with 4 piping elements into the primary flow nozzle.

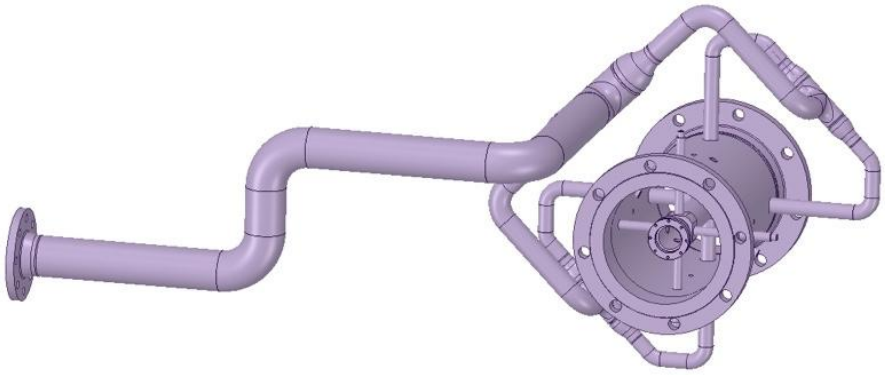

Figure 4-7 CAD model of feed line and manifold

Figure 4-8 Feed line and manifold in setup

4.2.5 Spool Component

The spool section is one of the critical sections of the setup because the chevron nozzle is positioned inside this part, and the mixing is initiated inside it. Its geometry has an essential role in the mixing process. In this setup, a constant area is designed for the spool section; thus, a constant area mixing process is performed. Also, the position of the chevron nozzle is specified by the nozzle exit position (NXP) criteria, which is one of the performance criteria. To observe the effect of the spool section, the spool component is removed from the test setup, and some experiments are performed without this part.

Figure 4-9 CAD model of the spool component

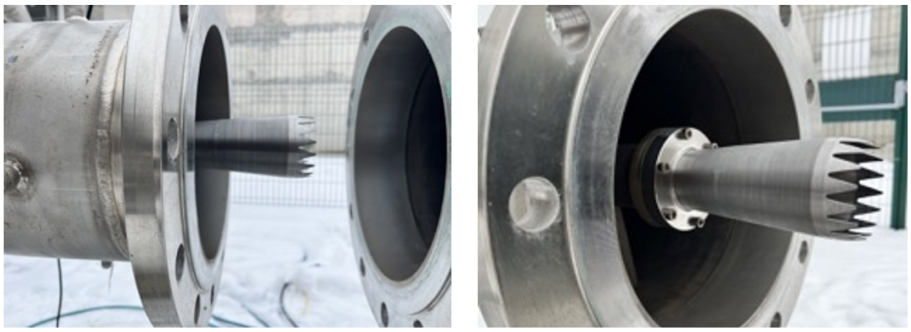

Figure 4-10 Mounted chevron nozzle inside of spool component in setup

4.2.6 Ejector-Diffuser Component

The ejector-diffuser is the core part of the experiment. It is mounted to the system between the transition cone and subsonic diffuser, and the mixing process details are investigated in this section. The most critical parameters for this section are the length and diameter of the ejector. In this study, due to test setup limitations, ejector diameter cannot be changed, but length can be changed because of its modular structure. The effect of L/D on the system's performance is examined by shortening and extending the structure.

Figure 4-11 CAD model of ejector-diffuser

Figure 4-12 Ejector-Diffuser section in setup

Figure 4-13 Ejector-Diffuser section's body component in setup

Figure 4-14 Diffuser-1 and Diffuser-2 components in setup

4.2.7 Subsonic Diffuser Component

The Subsonic Diffuser is the last element of the experimental setup. The mixed flow reduces its velocity and leaves the test setup.

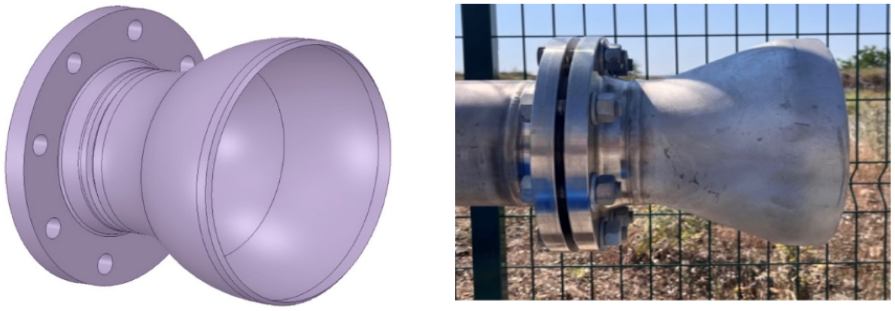

Figure 4-15 CAD model and setup component of subsonic diffuser

4.3 Measurements

The pressure data is measured from different points of the experiment setup. To understand the vacuum level, test chamber and diffuser pressures are critical, and data from these components are used to calculate the system's performance. There are 4 points on top of the test chamber. Pressure transducers are integrated at the P1 and P2 points. Also, thermocouples are integrated at T1 and T2 points, but temperature data are not used in this thesis study. Pressure data are also measured from P3 and P4 points for the ejector-diffuser section.

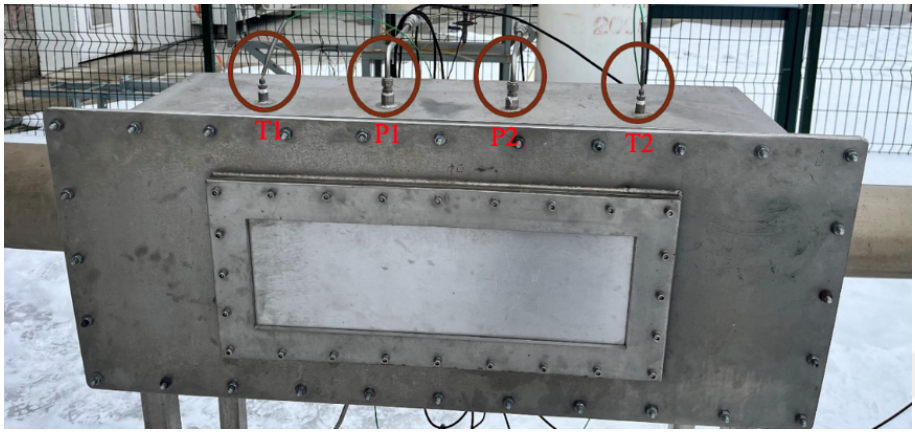

Figure 4-16 Measurement devices on top of test chamber

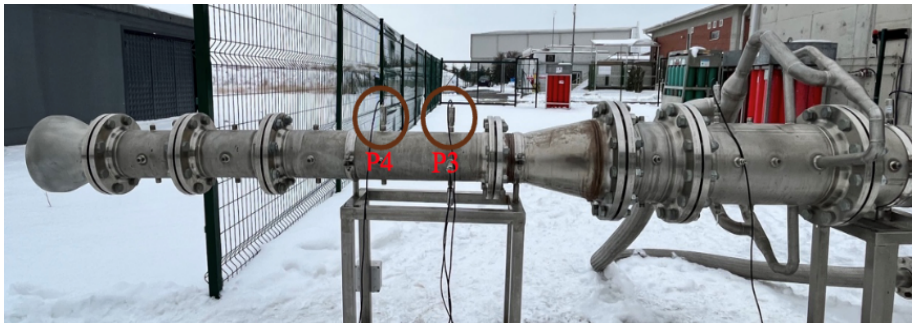

Figure 4-17 Measurement devices on top of ejector-diffuser body section

The experiment data is measured with the help of some special devices.

- Mass Flow Rate is measured by SAGE 200 thermal mass flow meter.
- Pressure data is measured by KISTLER 4260 A transducer.

4.3.1 Mass Flow Rate Measurement

The test setup's valve opening ratio regulates the air's mass flow rate. However, the mass flow rate must be tracked because of the pressure drop in long pipelines downstream of the free-jet nozzle. The SAGE 200 thermal mass flow meter measures the mass flow rate through a free-jet nozzle. At a rate of 1Hz, the data is recorded.

Figure 4-18 The SAGE 200 thermal mass flow meter

4.3.2 Pressure Measurement

In the experiment, pressure data is recorded by KISTLER 4260 A transducers with piezo-resistive 0-1 bara and 0-35 bara transducers in different setup sections. The recording rate is 25 kHz. The pressure data is recorded from the test chamber and ejector diffuser.

Figure 4-19 KISTLER 4260 A pressure device

4.4 Experiment Process Details

In the experimental study, some design parameters are varied, and their effects on system performance are examined. These parameters are the mass flow rate of free jet flow, length of mixing duct, and NXP. At first, the geometry of the experimental setup is not changed. Yet, free jet flow, which enters the ejector diffuser at the secondary inlet, is operated in three different mass flow rates. Second, the geometry of the system is switched. The ejector diffuser section is divided into three parts, represented in Figures 4-13 and 4-14. In order, the sections are named as ejector body, diffuser-1, and diffuser-2. One by one, diffuser sections are removed, and the length of the ejector-diffuser structure is diminished. In this way, the L/D parameter's effect is investigated.

Figure 4-20 Test Case-4, setup configuration-1

Figure 4-21 Test Case-5, setup configuration-2

Third, the spool section is altered. As explained before, the spool part is the starting component of the mixing process, and the spool geometry makes the mixing process in a constant area. In the third part of the experiment, the spool component is removed. In this way, the mixing process is initiated in a transition cone with varied

areas, and its effect is studied. In the third part of the experiment, the ejector length is also switched again to ensure that the mixing performance criteria's source is spool or length.

Figure 4-22 Test Case-6, setup configuration-3

Figure 4-23 Test Case-7, setup configuration-4

Figure 4-24 Test Case-8, setup configuration-5

There is an additional experiment performed at the end. The free jet flow is disconnected, and only primary flow is passed inside the ejector, and its influence is observed.

Figure 4-25 Setup configuration of additional test

The test plan is summarized in Table 4-2. 1 represents that the component is mounted to the setup, and 0 means that the component is demounted.

Table 4-2 Test plan of the study

Test Case-ID	Test Configuration	Free-Jet Nozzle Mass Flow Rate (g/s)	Spool	Diffuser-1	Diffuser-2
Test Case-1	Mass Flow Rate-1	750	1	1	1
Test Case-2	Mass Flow Rate-1	1170	1	1	1
Test Case-3	Mass Flow Rate-1	1300	1	1	1
Test Case-4	Test Setup Configuration-1	1170	1	1	0
Test Case-5	Test Setup Configuration-2	1170	1	0	0
Test Case-6	Test Setup Configuration-3	1170	0	0	0

Test Case-7	Test Setup Configuration-4	1170	0	0	1
Test Case-8	Test Setup Configuration-5	1170	0	1	1

4.5 Schlieren Imagining

Schlieren imagining entails capturing images that describe the motion of fluids. The standard setup of an optical schlieren system involves using light emitted by a single collimated source directed onto or through a specific object. This thesis study uses three mirrors, one high-speed camera, and one light source in the Schlieren imaging setup. The Schlieren imaging setup is described in Figures 4-25 and 4-26.

Figure 4-26 Schlieren Imagining setup

Figure 4-27 Mirror positions of Schlieren setup

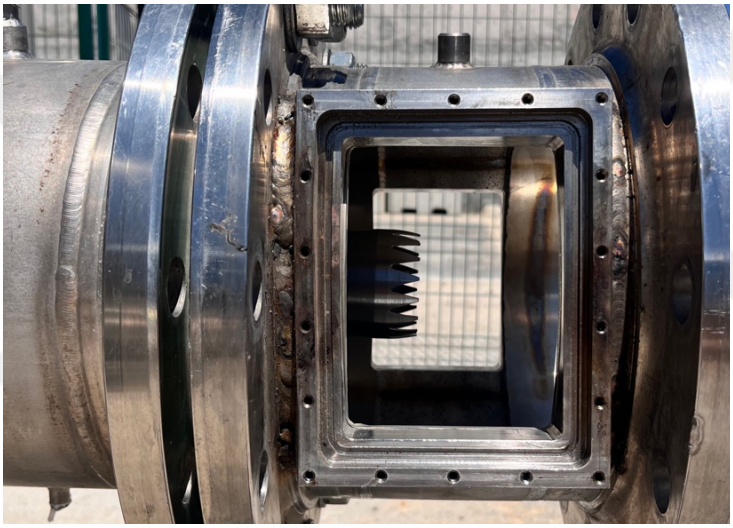

Figure 4-28 The spool component with a quartz glass opening

Due to the acquisition of Schlieren images at a significant level of detail and a rapid frame rate, typically measured in frames per second (fps), conducting video recording for a relatively short duration becomes possible. The experimental is performed again with Test Case-2 configuration, and the Schlieren image is saved to support the results using this visual result.

CHAPTER 5

RESULTS & DISCUSSION

5.1 Numerical Results

In this section, numerical results are represented. CFD study is performed by using the chevron nozzle, and its impact on the flow characteristic is investigated. Eight different cases are studied concerning operating conditions and geometry. The ejector-diffuser system geometry is unchanged in the first three cases, and the reference study's boundary conditions are applied. In Case 4, one diffuser section is removed, and in Case 5, two diffuser components are removed. Case 6 removes the spool section, and two diffusers remain demounted from the system geometry. In Case 7, the spool section is still demounted, and one diffuser section is added. At last, in Case 8, the spool section is removed, and two diffuser sections are added. The results are presented in two branches for eight cases: pressure distribution and Mach distribution.

5.1.1 Pressure Distribution

The mass flow rates are varied in the first three cases, and the pressure results are seen in Figures 5-1, 5-2, and 5-3. Mixing initiates at the spool section, characterized by a constant area, while the mixing duct comprises the ejector body and two diffuser sections. In this situation, the shock train originates before the mixing duct section. Due to the extended length, the shock train possesses adequate space to complete its progression. The pressure value to evaluate pressure recovery is the inlet pressure of the secondary flow. The secondary flow inlet pressures are measured as 29.3 kPa, 29.4 kPa, and 29.4 kPa.

The pressure distribution in the mixing duct is important to compare the numerical and the experimental results. In the experimental study, two transducers are mounted to the P3 and P4 points system to record the pressure data. The P3 point's position is selected in the numerical study, and the pressure data is calculated at that point. For Case 1, Case 2, and Case 3, P3 point pressure values are 39.1 kPa, 37.7 kPa, and 41.4 kPa.

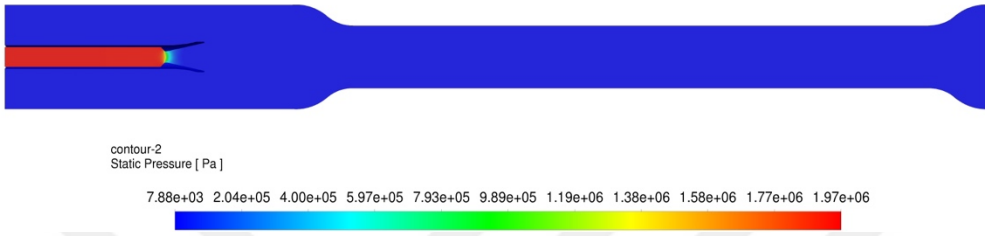

Figure 5-1 Pressure distribution of Case 1

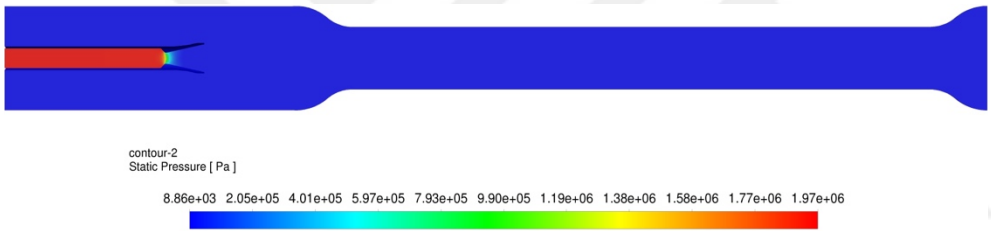

Figure 5-2 Pressure distribution of Case 2

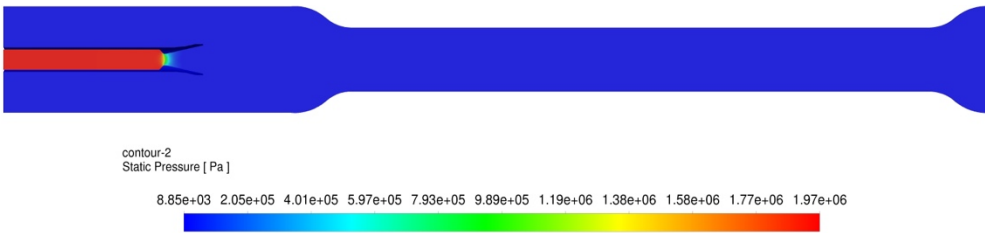

Figure 5-3 Pressure distribution of Case 3

In Case 4 and Case 5, the mixing duct length is changed, and its effect on the mixing is examined. The pressure results are calculated almost the same. There is a decimal difference between the results. The pressure values are 1953 kPa for the primary and 29.4 kPa for the secondary inlet. After the mixing, P3 point results are solved for two cases, and 2 kPa difference is observed in the pressure data. P3 point pressure is calculated as 40.4 kPa in Case 4 and 43.9 kPa in Case 5. These results show that

decreasing the length this much does not create a significant difference between results for constant area mixing configuration.

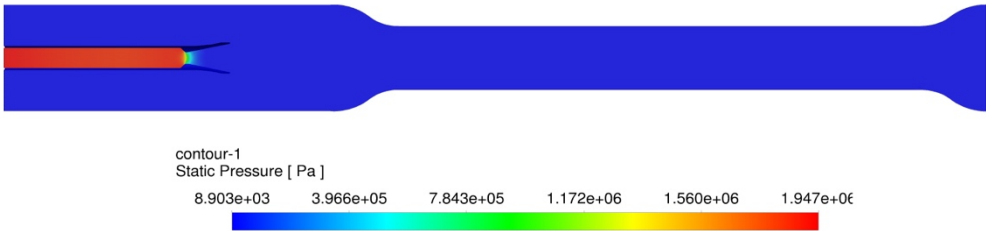

Figure 5-4 Pressure distribution of Case-4

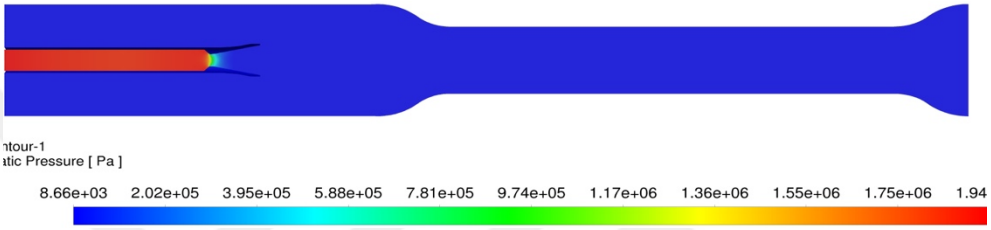

Figure 5-5 Pressure distribution of Case-5

In Case 6, the spool component is removed from the model and not mounted again for Case 7 and Case 8. Removing the spool component and changing the initiation area for the mixing affect the flow structure, as seen in Figures 5-6 to 5-8. The diamond shock appearance becomes obvious for these configurations, and the pressure distribution is impacted. To evaluate the effects of variable area mixing on the pressure, P3 point pressure values are also compared, and for Case 6, the pressure value is 50.7 kPa. For the flow inlets, the pressure results are 1954 kPa for the primary inlet and 29.7 kPa for the secondary inlet.

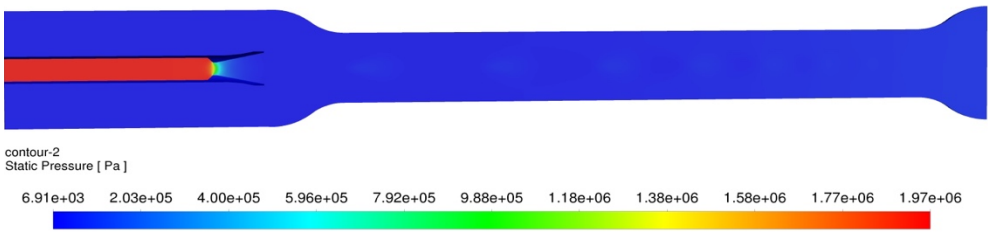

Figure 5-6 Pressure distribution of Case-6

The pressure values calculated for Case 7 and Case 8 are 31 kPa and 30.1 kPa in the P3 point. For the inlet conditions, the pressure values are almost the same. There are decimals between them. The pressure results are 1953 kPa for the primary inlet and 29.4 kPa for the secondary inlet in Case 7. Case 8's pressure results are 1954 kPa for the primary inlet and 29.4 kPa for the secondary inlet.

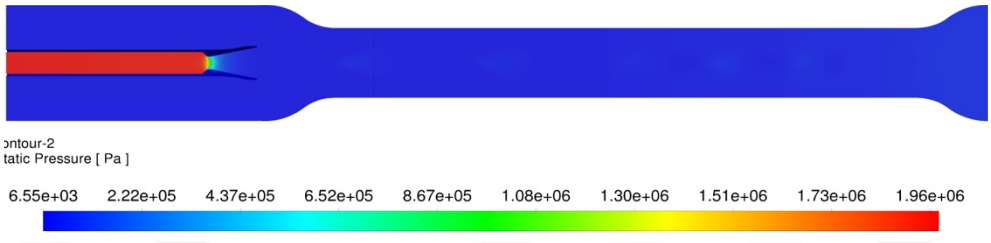

Figure 5-7 Pressure distribution Case-7

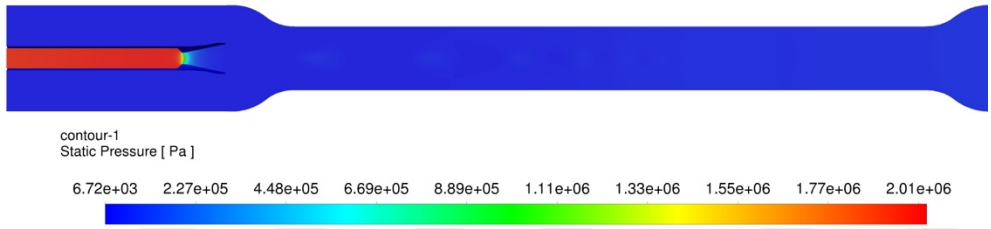

Figure 5-8 Pressure distribution of Case-8

5.1.2 Mach Distribution

In this part, the results of flow structure due to Mach variation for each numerical model are represented. First, to explain the flow structure in detail, Case 2 is highlighted in Figure 5-9, which has the same condition as the reference study and Schlieren setup.

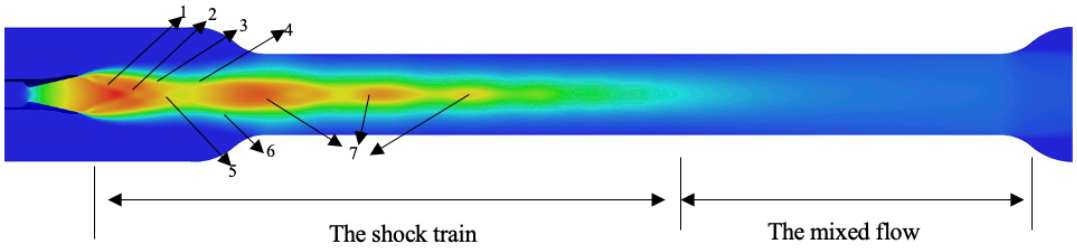

Figure 5-9 The flow structure of ejector-diffuser system

The flow structure is mainly divided into two sections: the shock train zone and the mixed flow zone. The shock train zone comprises the compression and reflected shock waves. The shock begins to compress internally and becomes the appearance of an oblique shock. Within the mixing duct, the compression wave crosses one another, and as a result of the compression waves coalescing, shock waves form in the jet. Merging oblique waves generates a triple point and a Mach disk. They are illustrated in Figure 5-9. Arrow 1 is for compression shock, and arrow 2 is for reflected shock. Also, the Mach disk exists as a normal shock after every diamond, represented by arrows 5 and 7. The position of the Mach disk is vital because it impacts the pressure distribution of the jet.

Further downstream, the shock patterns progressively began to disappear because of viscous dissipation along the free jet boundary layer which is seen with arrow 6 in Figure 5-9. The shock chain length is an important design criterion for performing efficient mixing. There should be sufficient chain length to complete the compression procession and mix two streams entirely. Moreover, the primary jet core zone size affects the vacuum performance seen in arrow 3. The proper jet core size determines the opening for the secondary flow to suck into the mixing duct. It is separated from the free jet boundary layer with the shear layer, illustrated with arrow 4 in Figure 5-9. These flow structure parameters specify the system performance, and for this thesis study, the results are evaluated by considering these topics.

The CFD study results are represented in Figures 5-10 to 5-17 and are explained based on their flow structures. Three different mass flow rates are applied in Figures

5-10 to 5-12. The change in the jet core is clearly in the results. Case 1 has the lowest secondary mass flow rate and largest jet core area. As explained in section 1.2.2.1, expanding the jet core causes a decrease in the annulus effective area and the amount of secondary flow that can be vacuumed. The mass flow rates of the secondary inlet for the first three cases are 0.33 kg/s, 0.532 kg/s, and 0.585 kg/s. In addition, the mass flow rates of the primary inlet for the first three cases were 1.422 kg/s, 1.425 kg/s, and 1.582 kg/s.

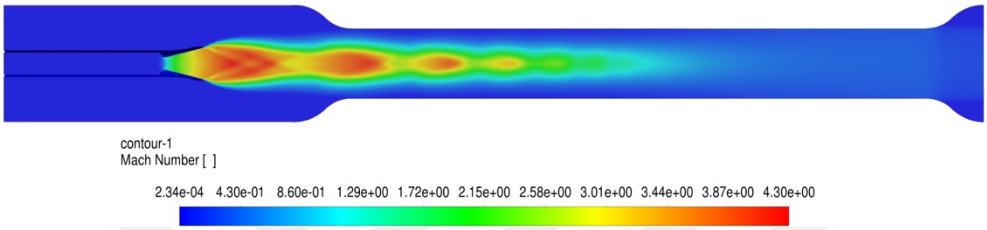

Figure 5-10 Mach distribution of Case-1

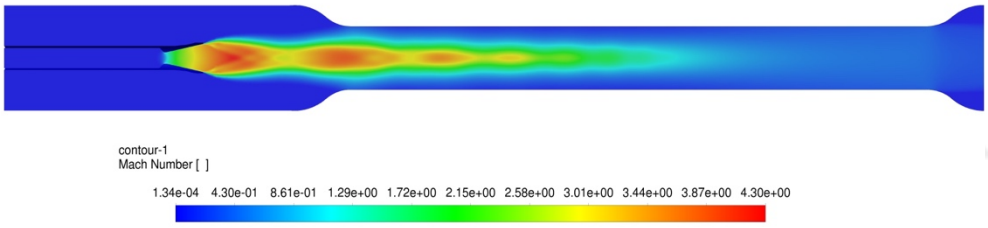

Figure 5-11 Mach distribution of Case-2

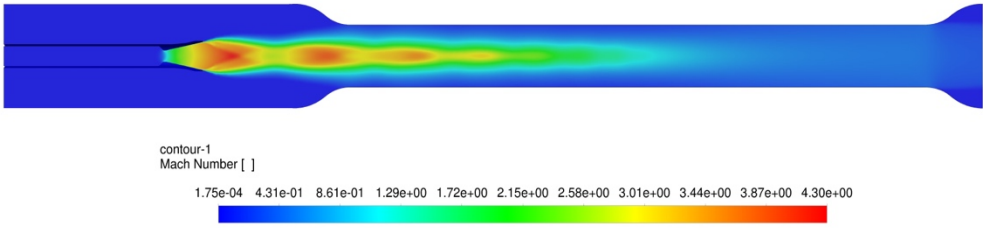

Figure 5-12 Mach distribution of Case-3

In Case 4 and Case 5, the mixing duct's length is decreased, affecting the flow structure. For these cases, the beginning of the oblique shock wave angle is changed compared to Case 2, which changes the Mach disk position. Also, the jet core structure is altered, affecting the mixing area's size. There should be enough zone to accomplish the mixing process so that higher flow can be sucked into the mixing

duct. The mass flow rates of the secondary inlet for the two cases are 0.61 kg/s and 0.59 kg/s. In addition, the mass flow rates of the primary inlet for the two cases were 1.51 kg/s and 1.59 kg/s. It shows that a small shortening in length does not generate a large difference in the mass flow rates for constant area mixing configuration. Also, the results imply no linear connection between the entrainment effect and the mixing duct length. There should be optimization to get the best performance.

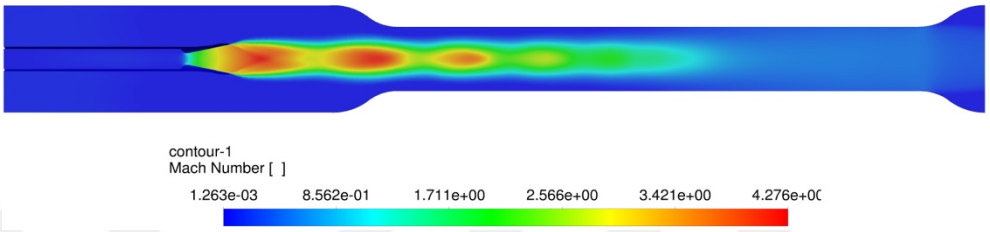

Figure 5-13 Mach distribution of Case-4

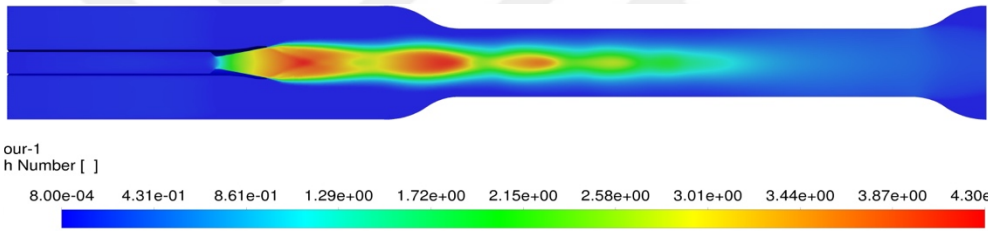

Figure 5-14 Mach distribution of Case-5

In Case 6, the spool part is removed from the model, and it causes the mixing is not initiated in the constant area. As seen in Figures 5-15, 5-16, and 5-17, the jet core flow structure is changed, especially the shock train length. It is observed that the oblique shock wave angle is changing, affecting the merge point of the waves far from the nozzle exit. It results in extending the shock train, affecting the ending of the mixing process. Case 6 has a long shock train length but the largest primary jet core, so it has the lowest vacuum performance. For Case 7 and Case 8, the only changed parameter was the length, but the change in the diamond wave structure is more than in Case 4 and Case 5. This shows that the initiation geometry of mixing (constant area or variable area) impacts the shock train structure and the vacuum performance. Case 7 has a smaller jet core and a longer shock train length. Due to the longer shock train length, the compression and mixing process is performed

efficiently, and there is a sufficient zone to vacuum secondary flow because of the smaller diameter on the jet core. Thus, Case 7 has a better performance. Case 8 completes the shock train in a shorter length, which means that the mixing and compression is not completely efficient, so it is a worser configuration than Case 7 to increase performance. The mass flow rates of the secondary inlet for the sixth, seventh, and eight cases are 0.41 kg/s, 0.452 kg/s, and 0.496 kg/s. In addition, the mass flow rates of the primary inlet for the sixth, seventh, and eighth cases are 1.425 kg/s, 1.28 kg/s, and 1.508 kg/s. The results prove the flow structure details.

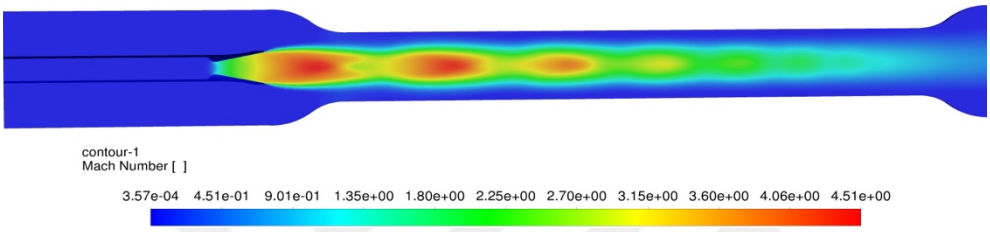

Figure 5-15 Mach distribution of Case-6

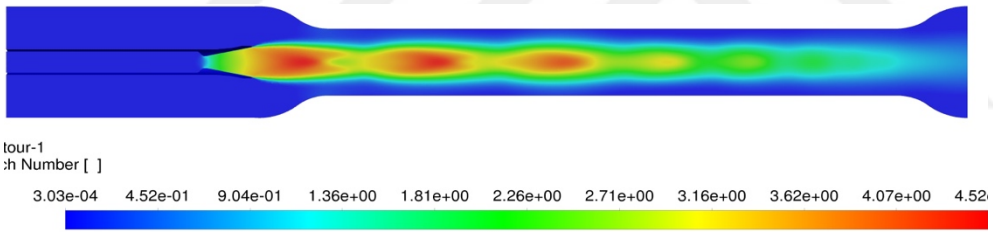

Figure 5-16 Mach distribution of Case-7

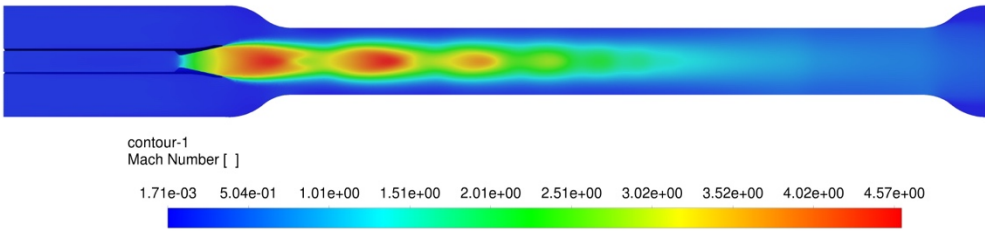

Figure 5-17 Mach distribution of Case-8

CFD results are summarized and represented in Table 5-1 based on pressure, mass flow rate and entrainment ratio.

Table 5-1 The summarized CFD results for chevron design

CFD Result Case-ID	Primary Inlet Mass Flow Rate (kg/s)	Secondary Inlet Mass Flow Rate (kg/s)	Entrainment Ratio (ER)	Mixing Duct P3 Point Pressure (kPa)
Case-1	1.422	0.33	0.232	39.1
Case-2	1.425	0.532	0.373	37.7
Case-3	1.582	0.585	0.37	41.4
Case-4	1.51	0.61	0.4	40.4
Case-5	1.59	0.59	0.371	43.9
Case-6	1.425	0.41	0.287	50.7
Case-7	1.28	0.452	0.353	31
Case-8	1.508	0.496	0.33	30.1

5.2 Experimental Results

In this section, eight different experimental results are represented. Four different pressure results are presented as pressure-time graphs for each test. The graphics are prepared using pressure data from P1, P2, P3, and P4 points. The experimental results are explained in two sections. The results of the P1 point from the test chamber and the P3 point from the mixing duct are shown with pressure-time graphs in sections 5.2.1 and 5.2.2. Test chamber pressure results are compared with the reference result to control the difference between solutions and to understand the chevron influence on the vacuum. P2 and P4 points pressure-time graphs are shown in the Appendix A. Oscillations are occurring for pressure data due to flow conditions and the sensitivity of experiment measurement devices. The vibration and

the supersonic transient flow conditions are the reasons for the oscillations in the pressure data. Thus, the filtered mean pressure data is represented with figures and tables.

5.2.1 Pressure Result from Test Chamber

Significant oscillations are observed in the first test, and it does not stabilize. The pressure data still needs to be stable, but the averaged pressure data from the Test Chamber P1 point is taken at the 100th second, approximately **9.89 kPa.** After the 155th second, due to the decrease in mass flow rate, a sudden jump in the pressure is obtained, and the test is finalized. Due to the chevron effect, it was expected that test chamber pressure would be lower than 3800 Pa, which is the reference study pressure data, but the results show that the pressure data is much higher; thus, this configuration is not preferable option for high-performance ejector-diffuser system.

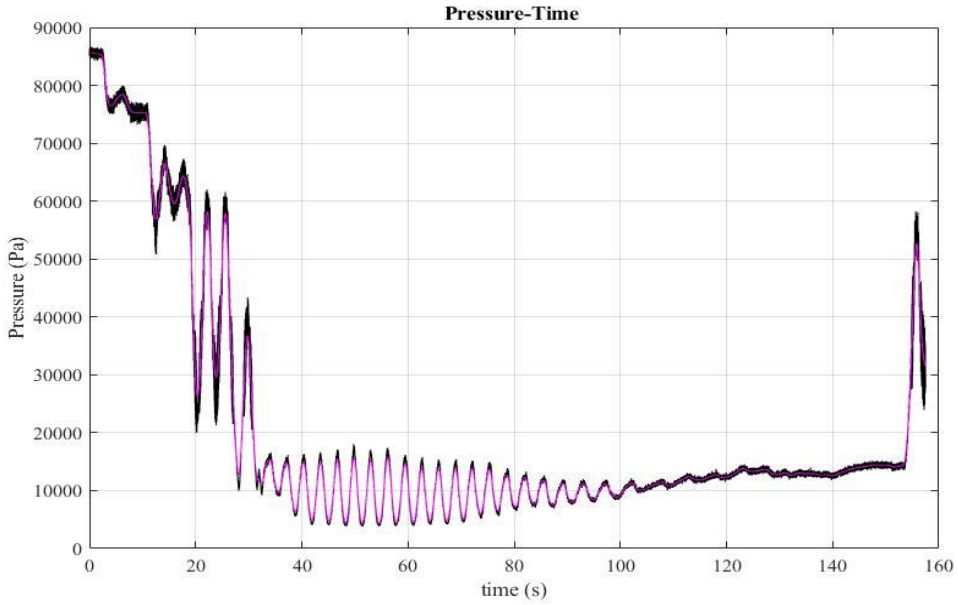

Figure 5-18 Pressure-time variation of Case-1 in the test chamber

In the second test, oscillations are also observed, and the pressure data is stabilized almost at the 75th second. The filtered mean pressure data from Test Chamber P1 point is taken at the 75th second, measuring approximately **5748.9 Pascal.** After the

170th second, due to the decrease in mass flow rate, a sudden jump in the pressure is obtained, and the test is finalized. Altering the free-jet mass flow rate changed to the test chamber pressure. Due to the chevron effect, it was expected that the test chamber pressure would be lower than 5900 Pa, which is the reference study pressure data, and the results show that the goal of the chevron is accomplished.

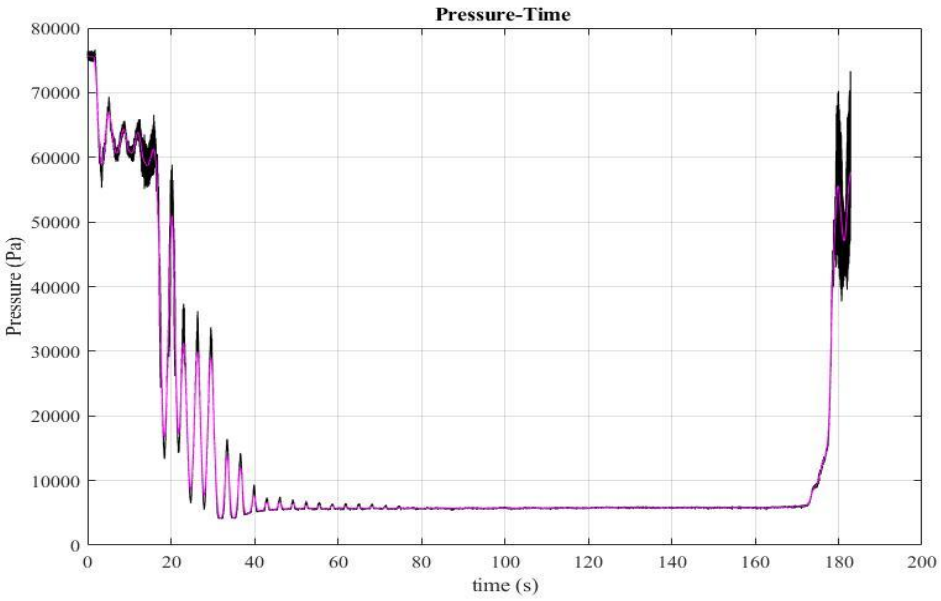

Figure 5-19 Pressure-time variation of Case-2 in the test chamber

In the third test, the pressure data is stabilized almost at the 40th second, earlier than the first two tests. Increasing the free jet mass flow rate results in an undesired elevation of the test chamber pressure. The filtered mean pressure data from Test Chamber P1 point was saved at the 40th second, calculating approximately 6468.9 Pascal. Due to the chevron consequence, the test chamber pressure was expected to be lower than 6800 Pa, the reference study pressure data. The results show that the pressure data is much lower; thus, the goal of the chevron is accomplished.

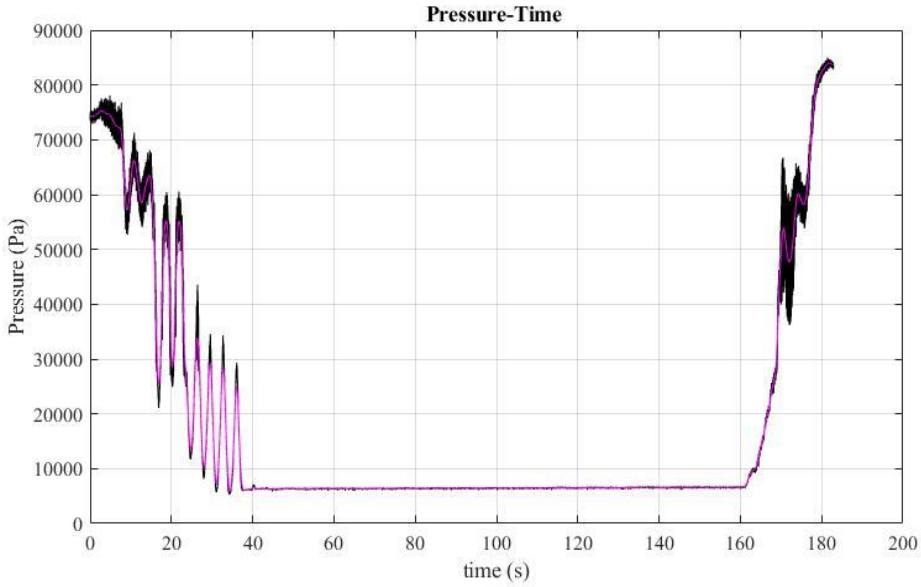

Figure 5-20 Pressure-time variation of Case-3 in the test chamber

In the fourth test, oscillations are also observed, and the pressure data is stabilized nearly at the 50th second. Lessening the mixing area causes alterations in vacuum performance, subsequently affecting the test chamber pressure. The filtered mean pressure data from Test chamber P1 point was recorded at the 50th second, an approximate value of **5681.63 Pascal.** After the 160th second, due to the inadequate mass flow supply, a sudden jump in the pressure is obtained, and the test is completed. Due to the chevron impact, it was expected that the test chamber pressure would be lower than 5900 Pa, which is the reference study pressure data, and the results demonstrate that the goal of the chevron is accomplished.

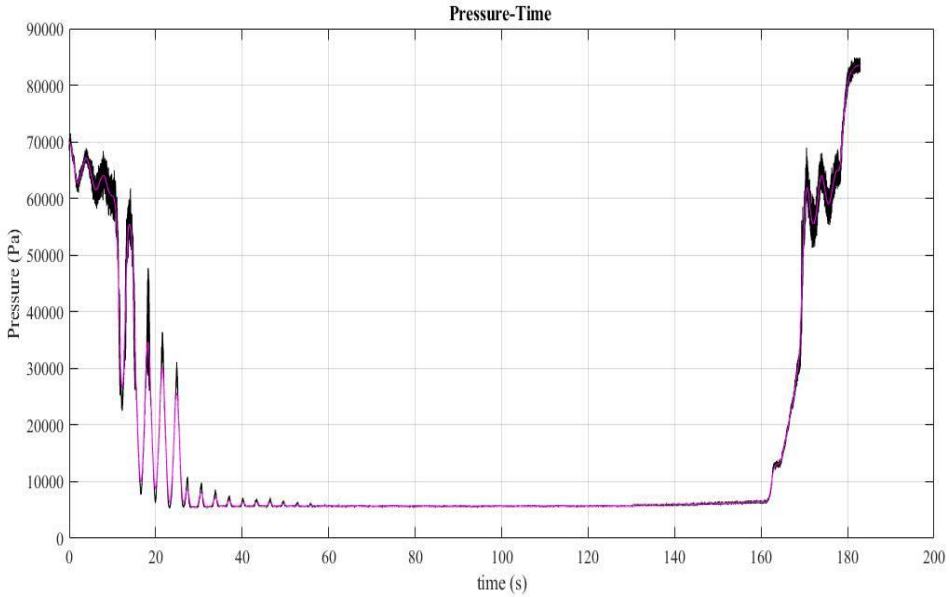

Figure 5-21 Pressure-time variation of Case-4 in the test chamber

In the fifth test, the pressure data is stabilized almost at the 80th second. Reducing the mixing area adversely affects the vacuum performance, subsequently affecting the test chamber pressure. The filtered mean pressure data from Test Chamber P1 point is calculated at the 80th second, approximately **6690 Pascal**. The results of the test chamber pressure demonstrate an undesired increase due to the reduction in mixing area length. This guides that the length-to-diameter (L/D) ratio is a considerable parameter for achieving effective vacuum performance, and its optimization is essential to identify the appropriate value for achieving expected results.

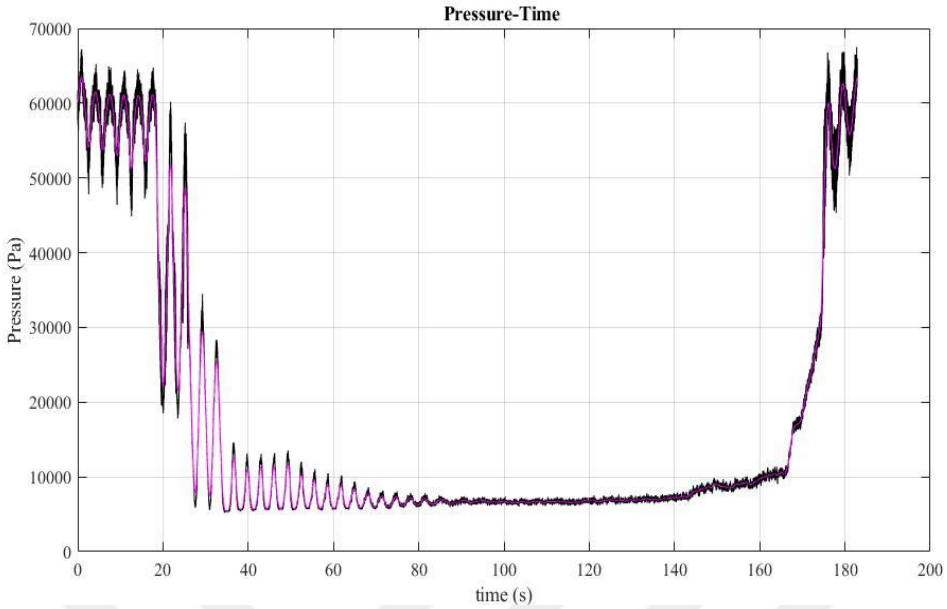

Figure 5-22 Pressure-time variation of Case-5 in the test chamber

In the sixth test, more significant oscillations are observed, and it only stabilizes in the 120th second. The pressure data still needs to be regular, but the averaged pressure data from Test Chamber P1 point is taken at the 120th second, approximately **20569.75 Pascal.** Significant and unexpected changes are observed in the test chamber component due to the reduction of the spool section. The results exhibit pressure values that fall outside the expected ranges. This configuration is not proper to enhance vacuum performance and should be avoided.

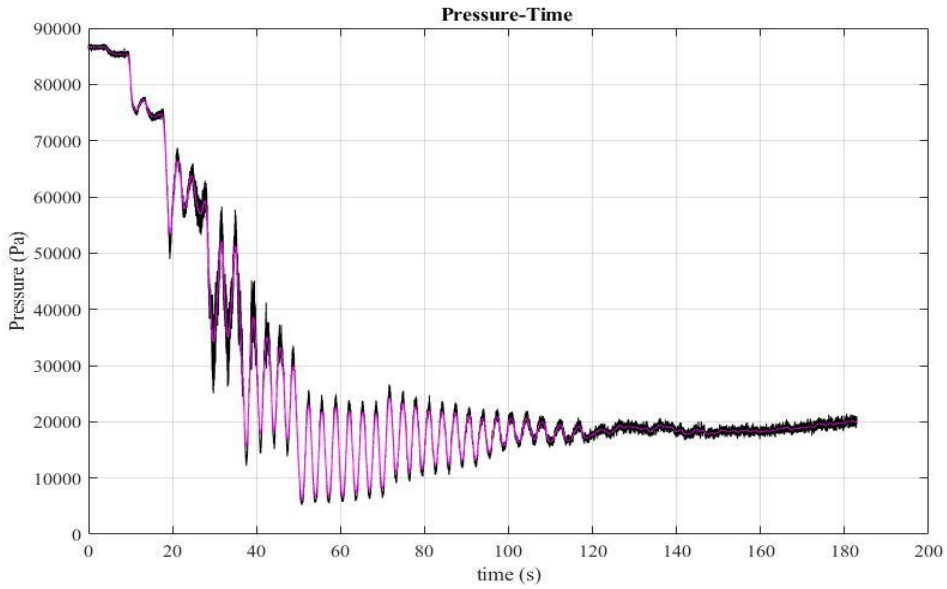

Figure 5-23 Pressure-time variation of Case-6 in the test chamber

In the seventh test, the pressure data is stabilized almost at the 90th second. Adding a diffuser component and extending the mixing length produce better results than the sixth test. This configuration generates pressure outcomes in the test chamber close to those observed in fourth test. The filtered mean pressure data from Test Chamber P1 point is measured at the 90th second, approximately **5632.785 Pascal.**

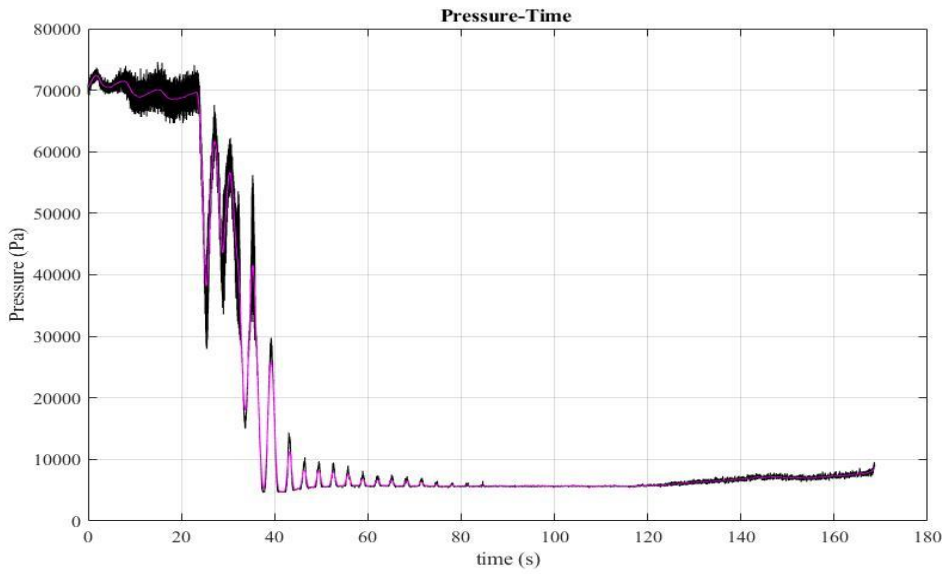

Figure 5-24 Pressure-time variation of Case-7 in the test chamber

In the eighth test, the pressure data is stabilized almost at the 70th second. It has been detected that the test chamber pressure has increased when compared to the seventh test. The filtered mean pressure data from the Test Chamber P1 point was saved at the 70th second, with an approximate value of **5877 Pascal**. This case demonstrates an optimal mixing length to achieve the highest vacuum efficiency. Consequently, it emphasized optimizing the length-to-diameter (L/D) ratio.

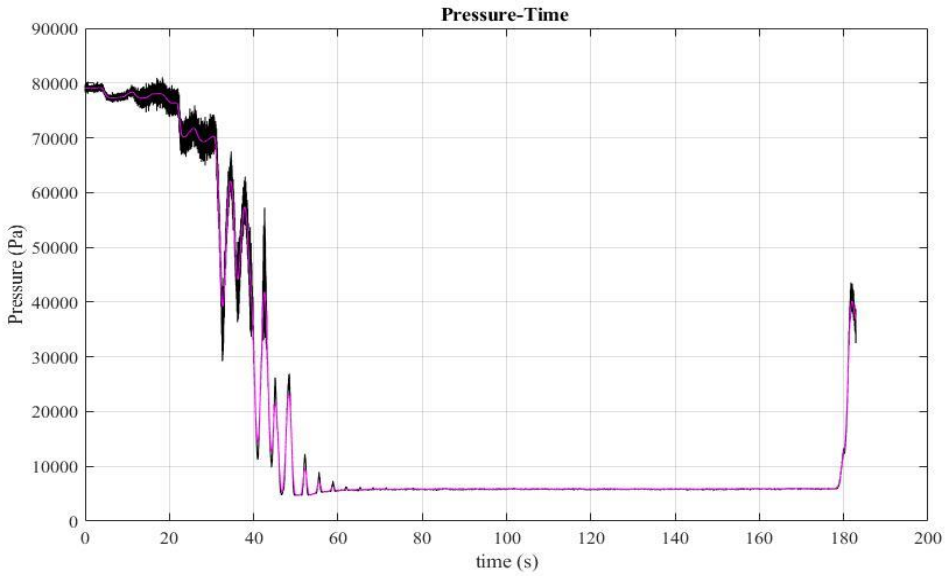

Figure 5-25 Pressure-time variation of Case-8 in the test chamber

5.2.2 Pressure Result from Mixing Duct

The pressure results from the mixing duct have higher oscillations than the one in the test chamber. P3 point pressure data is vital to compare and validate the numerical solution with the experiment.

In Case 1, the mean pressure data is not entirely stable. The filtered mean pressure data from the P3 point is taken at the 100th second, approximately as **47.9 kPa**. In the CFD solution for Case 1, pressure in the P3 point is calculated as **39.1 kPa.**

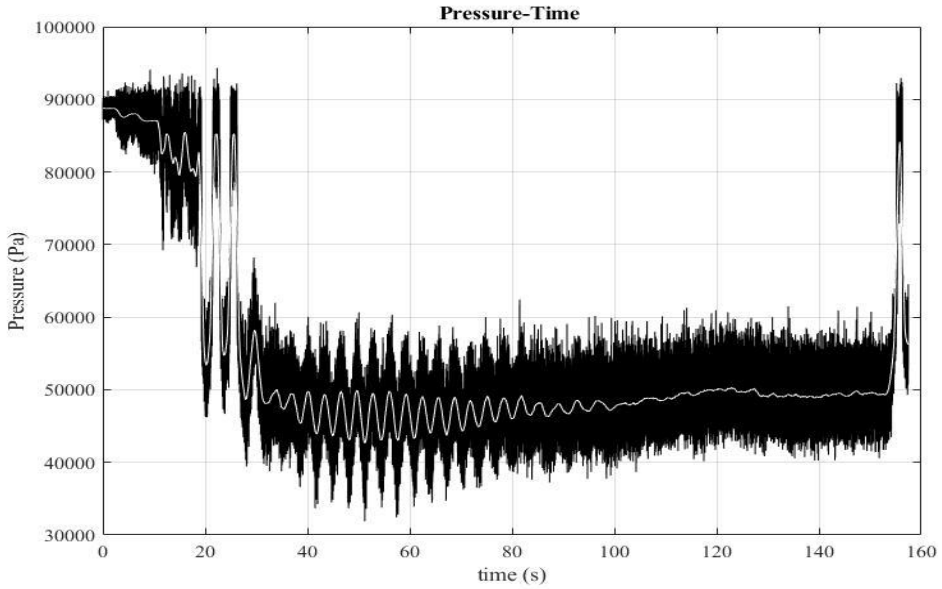

Figure 5-26 Pressure-time variation of Case-1 in the mixing duct

In Case 2, the range of oscillations is smaller than Case 1. The filtered mean pressure data from the P3 point is taken at the 100th second, approximately as **41.07 kPa**. In the CFD solution for Case 2, pressure in the P3 point is calculated as **37.7 kPa.**

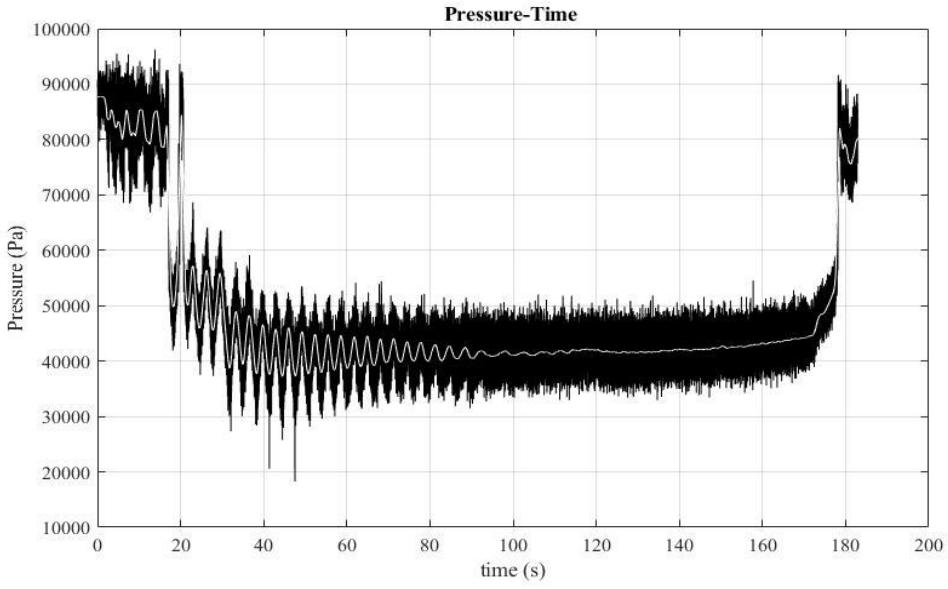

Figure 5-27 Pressure-time variation of Case-2 in the mixing duct

In Case 3, the oscillations are still higher than the ones in test chamber data, but the range of oscillations is narrower than in Case 1 and Case 2. The filtered mean pressure data from the P3 point is taken at the 100th second, approximately as **42.7 kPa**. In the CFD solution for Case 3, pressure in the P3 point is calculated as **41.4 kPa.**

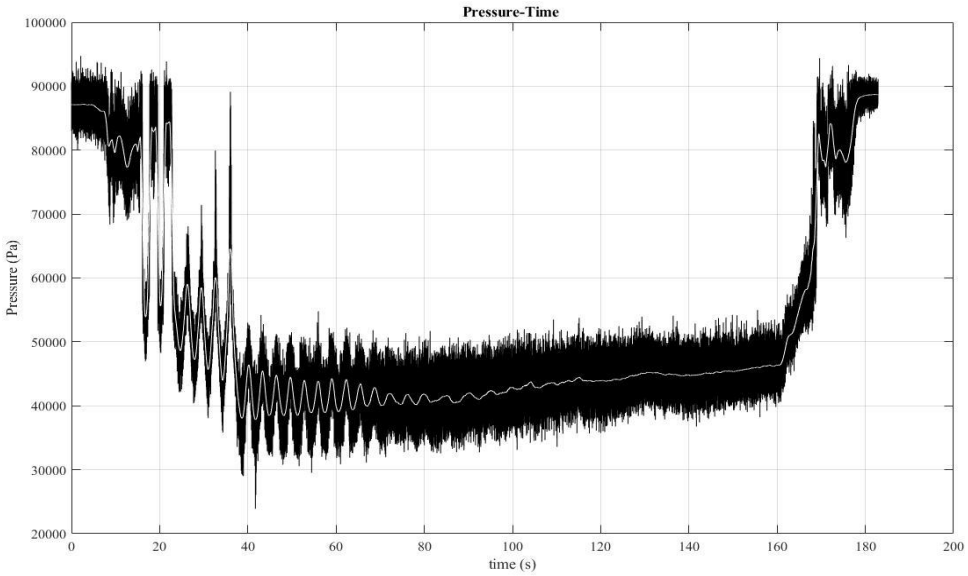

Figure 5-28 Pressure-time variation of Case-3 in the mixing duct

In Case 4, the mean pressure data is more stable. The filtered mean pressure data from the P3 point is taken at the 100th second, approximately as **41.6 kPa**. In the CFD solution for Case 4, pressure in the P3 point is calculated as **40.4 kPa.**

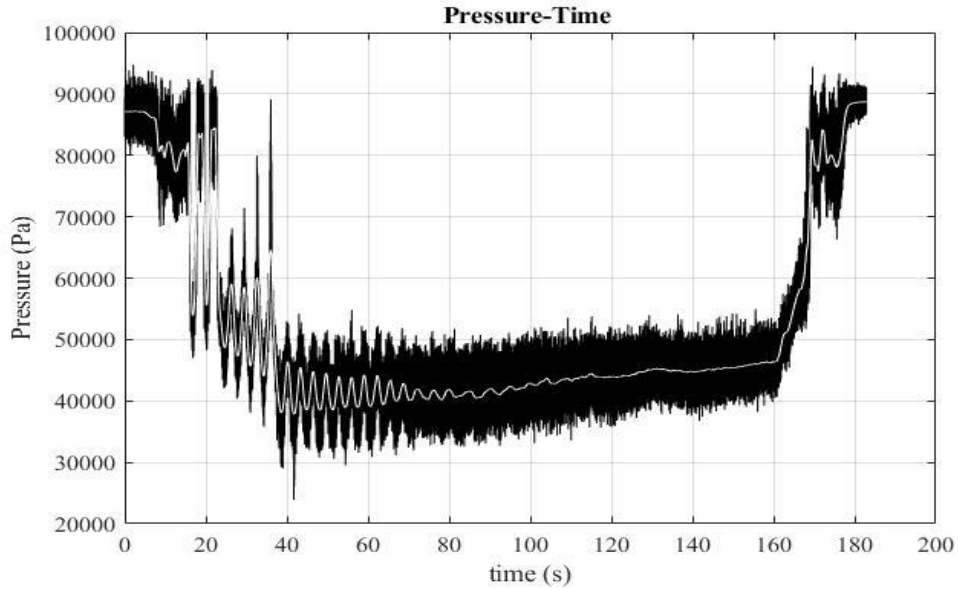

Figure 5-29 Pressure-time variation of Case-4 in the mixing duct

In Case 5, the mean pressure data is nearly stable after the 100th second. The filtered mean pressure data from the P3 point is taken at the 100th second, approximately as **48.6 kPa**. In the CFD solution for Case 5, pressure in the P3 point is calculated as **43.9 kPa.**

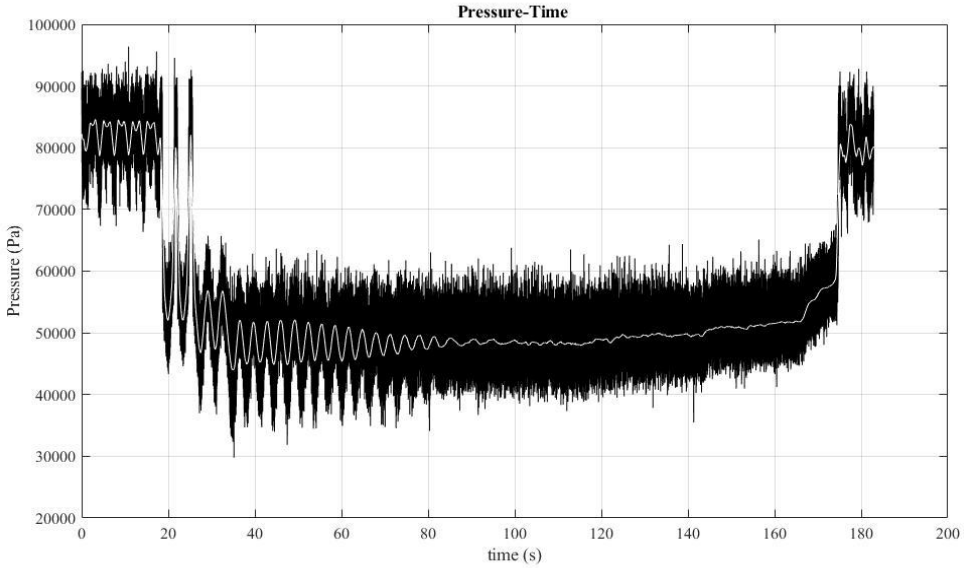

Figure 5-30 Pressure-time variation of Case-5 in the mixing duct

In Case 6, the mean pressure data is nearly stable after the 120th second. The filtered mean pressure data from the P3 point is taken at the 120th second, approximately as **52 kPa**. In the CFD solution for Case 6, pressure in the P3 point is calculated as **50.7 kPa.**

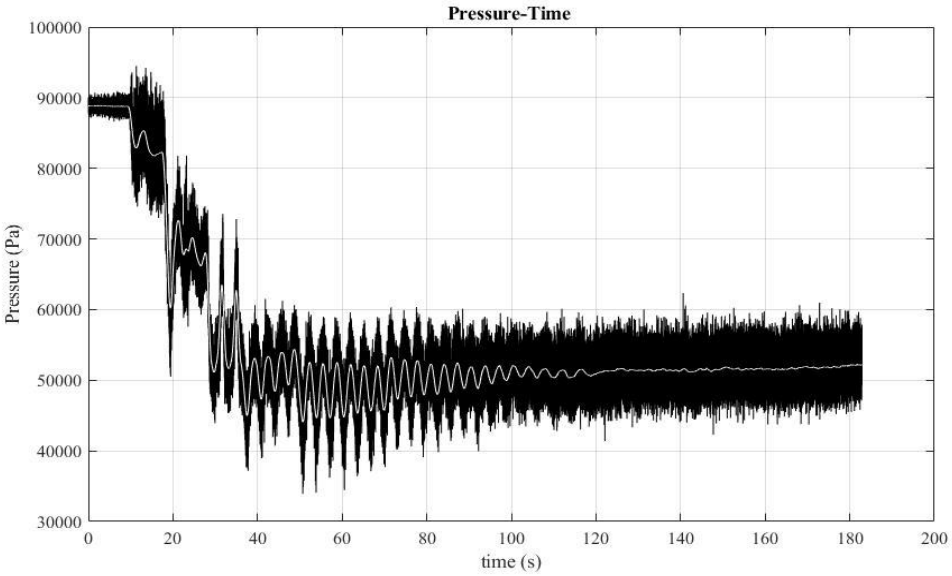

Figure 5-31 Pressure-time variation of Case-6 in the mixing duct

In Case 7, the mean pressure data is nearly stable after the 100th. The filtered mean pressure data from the P3 point is taken at the 100th second, approximately as **39.1 kPa**. In the CFD solution for Case 7, pressure in P3 point is calculated as **31 kPa.**

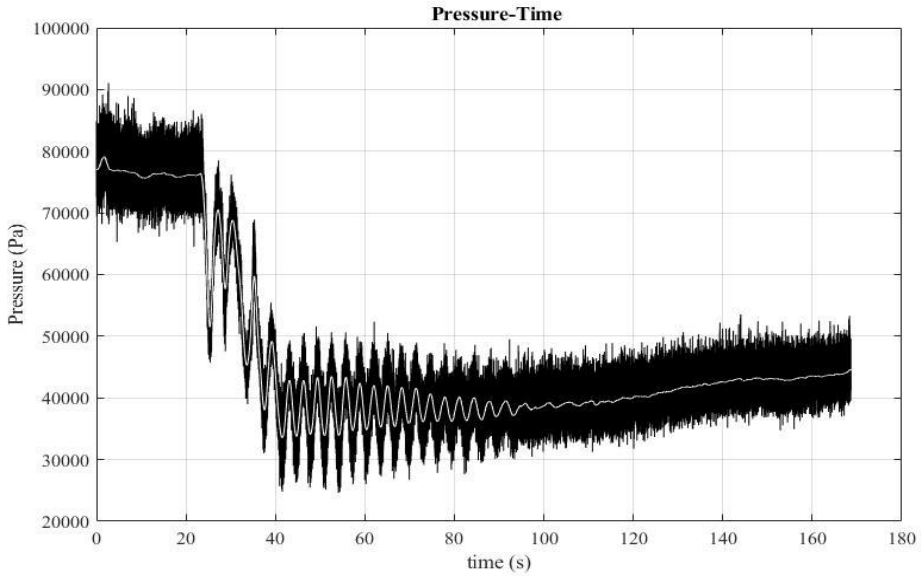

Figure 5-32 Pressure-time variation of Case-7 in the mixing duct

In Case 8, the mean pressure data is nearly stable after the 120th second. The filtered mean pressure data from the P3 point is taken at the 120th second, approximately as **34.4 kPa**. In the CFD solution for Case 8, pressure in the P3 point is calculated as **30.1 kPa.**

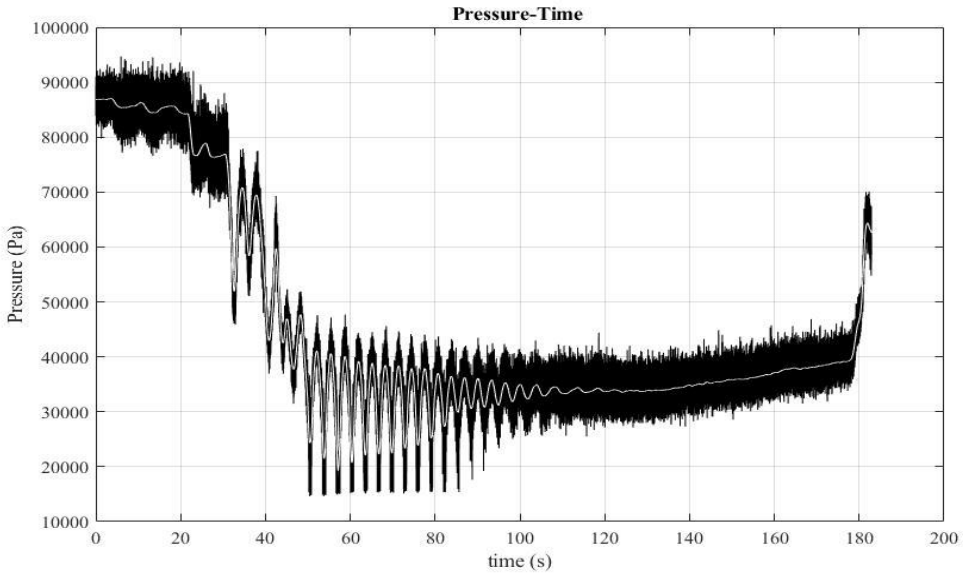

Figure 5-33 Pressure-time variation of Case-8 in the mixing duct

The results are summarized and represented in Table 5-2

Table 5-2 The summarized results of experimental study

Test Case-ID	Test Chamber P1 Point Pressure (Pa)	Test Chamber P2 Point Pressure (Pa)	Mixing Duct P3 Point Pressure (kPa)	Mixing Duct P4 Point Pressure (kPa)
Case-1	9888	10087	48	62.1
Case-2	5749	5944	41.07	52.28
Case-3	6468	6686	42.7	53.3
Case-4	5681	5885	41.6	52.7
Case-5	6690	6856	48.6	59.8
Case-6	20569	20724	52	61
Case-7	5632	5821	39.1	48.1
Case-8	5877	6070	34.4	43.1

5.3 Schlieren Imaging Results

The purpose of the Schlieren imaging is to visualize the mixed flow at the exit of the chevron nozzle. Before the process starts, the chevron nozzle without flow is seen in Figure 5-34.

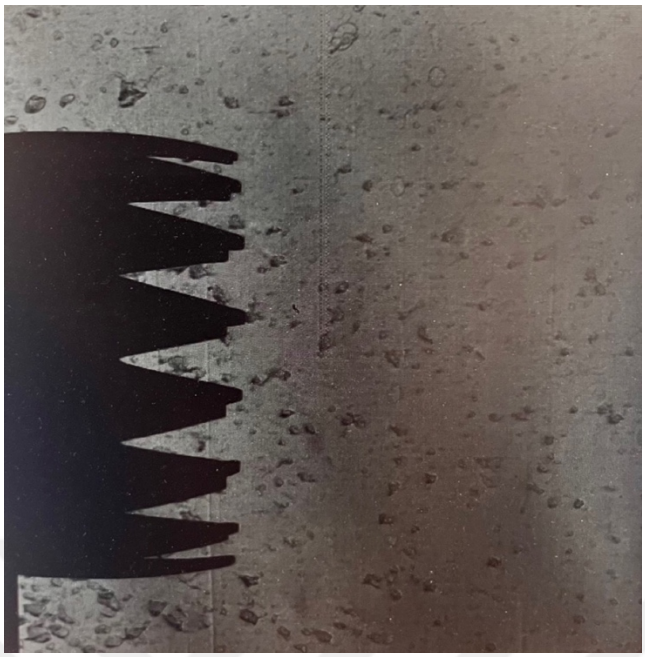

Figure 5-34 The chevron nozzle appearance from the high-speed camera

As seen in Figure 5-34 and 5-35, the high-speed camera focuses explicitly on the exit of the Chevron nozzle to capture the initiation of the mixing. Due to the asymmetric perspective, all chevron teethes can be seen. There are spots on the Schlieren image.

These spots on the quartz glass are because of the dust particles inside the spool component.

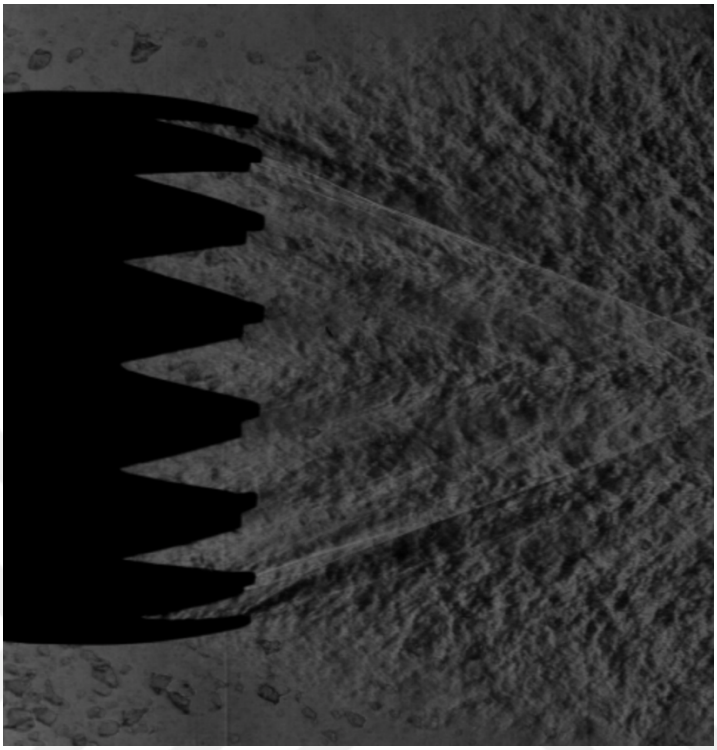

Figure 5-35 Schlieren image of mixed flow

The time-resolved visual result is represented in Figure 5-35. This Schlieren image allows us to investigate the mixing of two streams in a real case. Oblique shock waves resulting from the chevron structure and the initiation of the shock train are observable in this figure. The images of the generated shock waves overlap due to the three-dimensional nozzle model and the asymmetric perspective. However, the primary goal of Schlieren imaging in this thesis study is to enhance the understanding of mixing flow and shock train generation. With the assistance of this visual result, the objective is successfully achieved.

5.4 The Comparison of Numerical and Experimental Results

In this part, the results are compared with each other in two different ways. At first, the numerical results are validated using the Schlieren image in this part. Schlieren test is operated with the boundary conditions and the geometric configuration of Case 2. Thus, to compare the two results, Case 2 is selected. The purpose of the Schlieren image in this study is to support and visualize the CFD result; however, due to the limited area on the Schlieren image, only the primary nozzle exit, and the beginning of the shock train are used to compare.

In CFD results, the wave details are not precise individually, but their compression angle can be calculated, and their contact points can be describable. For the Schlieren result, compression and reflection waves can be seen clearly, but due to mirror positions, chevron nozzle teethes are not symmetric, generating a more complex view. As explained in section 5.1.2 and Figure 5.9, the shock begins with compression internally, and compression waves cross each other. In Figure 5-36, the beginning of the shock chain is framed for both results and while the shock waves are more obvious in the Schlieren image, the CFD result specifies the waves with their colored contour. The reflected waves are seen in both cases after the compression waves collide. The angle of the waves demonstrate that reflection waves are not strong enough to reach the duct wall and progress inside the jet core. This statement can be verified in CFD result by checking the ejector-diffuser system and the Schlieren image area can only shows the initial reflection angle. However, based on the initial compression and reflection waves, the rest of the shock train waves can be calculated manually which is so much costly. In the end, the flow structure is similar for both results, and the Schlieren image confirms the CFD result. To improve the results of section 5.4, Schlieren image area can be enlarged for the future studies.

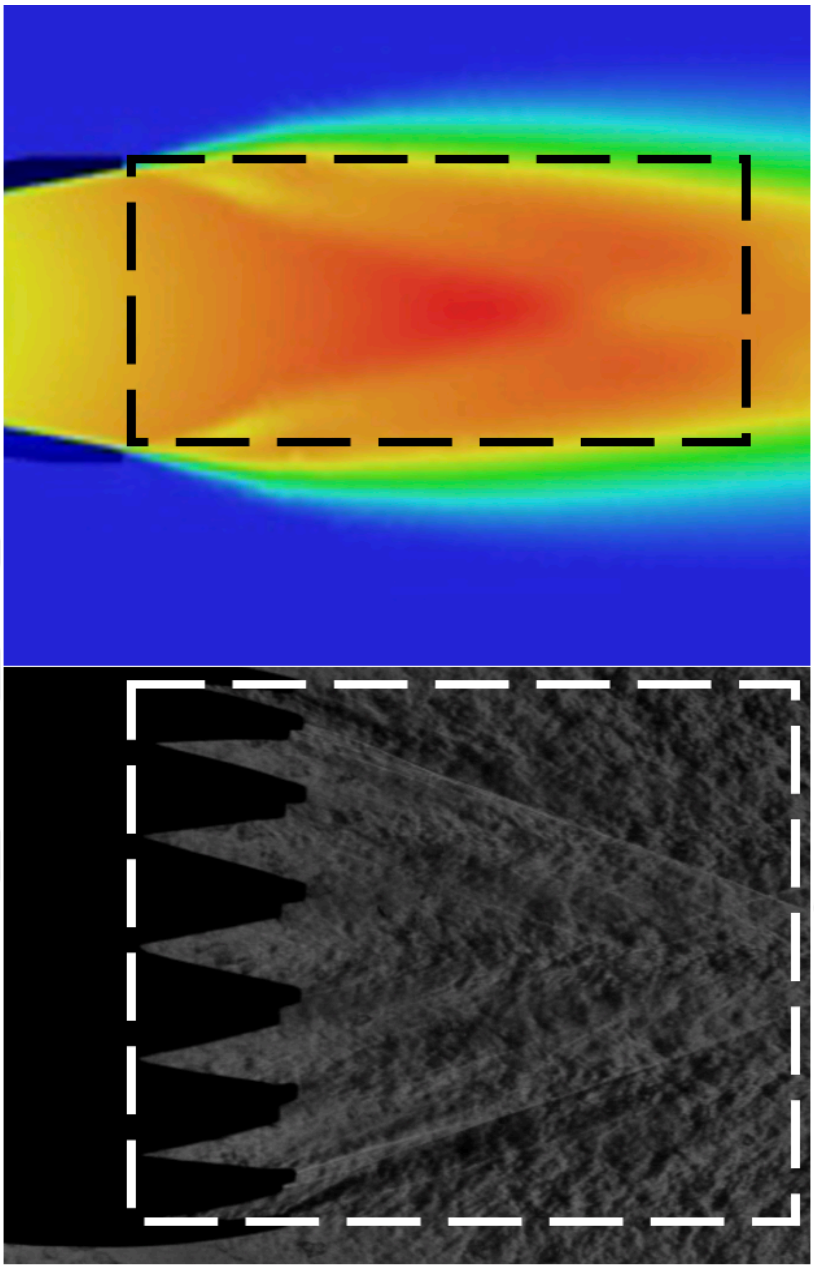

Figure 5-36 The comparison the numerical solution with Schlieren image

For Case 2, the numerical result is also validated with the experimental result. The common point for both study is the comparing pressure value in the mixing duct. In Case 2, the experimental result is approximately as **41.07 kPa** and the CFD result is **37.7 kPa**. The error calculation is performed by using equations 5.1.

$$\text{Error} = \left|\frac{(\text{Pressure})_{\text{CFD}} - (\text{Pressure})_{\text{Experiment}}}{(\text{Pressure})_{\text{Experiment}}}\right| \times 100 \qquad (5.1)$$

$$\text{Error} = \left(\frac{3.37}{41.07}\right) \times 100 = 8.2\%$$

It is seen that the results are very close to each other and the error between the results is lower than ten percent. In this way, the numerical result is validated with the experimental result for Case 2. For the rest of the cases, the same error calculations are performed, and they are represented in Table 5-3.

Table 5-3 The difference between the numerical and experimental results

Case-ID	The numerical study result (kPa)	The experimental study result (kPa)	Difference between results (Pa)	Error (%)
Case-1	39.1	48	8.9	18.5%
Case-2	37.7	41.07	4	8.2%
Case-3	41.8	42.7	0.9	2.1%
Case-4	40.4	41.6	0.2	3%
Case-5	43.9	48.6	4.7	9.7%
Case-6	50.7	52	1.3	2.5%
Case-7	31	39.1	8.1	20%
Case-8	31.2	34.4	3.2	9.4%

The error calculations show that the difference between the numerical and the experimental results is mostly lower than ten percent. The difference is almost twenty percent for the two cases, which is still not so high. The higher error level for those two cases could be due to the problems of the experimental process. In the first case, the mass flow rate is not stabilized, which may generate an error in the solution.

In addition, for the seventh case, the diffuser-1 component is mounted again into the setup, and during the mounting process, it may disrupt the structure's integrity and increase the error level. However, the overall error between both studies is not much, and it can be said that the experimental results validate the numerical results.

5.5 The Evaluation of the Results

In this section, the numerical and experimental results of a chevron nozzle are compared with those of a circular nozzle, and changes in performance are determined from two different perspectives. For the numerical results, the entrainment ratio, which represents the ratio of the mass flow rate of the secondary flow to the primary flow, will serve as the performance parameter. Regarding the experimental results, the vacuum effect will be the performance parameter, defined as the decrease in test chamber pressure. This approach allows for analyzing the chevron nozzle's performance using two criteria.

Firstly, the numerical results are compared. The ejector-diffuser system with a circular nozzle has approximately three kg/s of primary flow and one kg/s mass flow rate of secondary flow. According to Equation 1.1, the entrainment ratio is calculated, and it equals 0.33. It is expected that because of the vacuum effect of the chevron nozzle, the entrainment ratio should be higher than 0.33 in the ejector-diffuser system with a chevron nozzle.

In this thesis study, the ejector-diffuser system with a chevron nozzle is solved with half the geometry size. At the same time, to understand the effects of ejector geometry, the same boundary conditions are applied, and the entrainment ratios are calculated. The results are represented in Table 5-1.

The fundamental objective of this thesis study is to investigate the chevron effect on ejector performance. The ejector’s performance is evaluated in the CFD study by measuring the entrainment ratio. The ejector-diffuser system with a circular nozzle exhibited an entrainment ratio of 0.33. The CFD Case-2 configuration is suitable for

comparing the entrainment ratio, displaying an entrainment ratio of 0.373. This demonstrates that utilizing a chevron nozzle enhances the entrainment factor. With the same geometric arrangement, there is a 13 % increase in the entrainment ratio, which is further improved, as observed in CFD Case-2. Among the options, CFD Case-4 is selected as the optimal configuration for the ejector-diffuser system with a chevron nozzle due to its entrainment ratio of 0.4 With the CFD Case-4 configuration, the ejector-diffuser performance experiences a 21 % increase.

The second side of performance comparison is based on the vacuum performance. It is expected that using a chevron nozzle increases the vacuum performance, and thus, the test chamber pressure is decreased. The test chamber pressure was measured at 5900 Pa from the experiment results in the reference study. Test Case 2 has the same geometric setup and boundary condition in this study. In test case 2, the test chamber pressure is measured as 5749 Pa, as is seen in Table 5-3. It proves that test chamber pressure is decreased. The rest of the pressure values from the P1 point are examined to understand the best design option for the ejector performance. Table 5-3 shows that the test chamber has the lowest pressure values in Test Case-4 and Test Case-7, which are almost the same. It is assumed that the lowest pressure value of the test chamber is 5650 Pa, which means that using a chevron nozzle instead of a circular nozzle result in a 250 Pa decrease in the test chamber. It can be said that the vacuum level of the system has increased by nearly 4.25%, which is not an anticipated increase.

CHAPTER 6

CONCLUSION & FUTURE WORK

6.1 Conclusion

In this thesis study, the primary nozzle flow within the ejector system is investigated numerically and experimentally. The chevron nozzle is employed as the primary nozzle, and its effects on ejector performance are compared to a study with a circular nozzle.

To begin with, the ejector system with the chevron nozzle is numerically solved using a 3D model. Grid independence is assessed, and an appropriate mesh model is chosen to solve the problem. The ANSYS FLUENT software is the CFD solver tool, with relevant inputs defined within FLUENT. For comparison purposes, circular nozzle boundary conditions are defined. Additionally, the impacts of two critical geometric parameters are studied numerically: the nozzle exit position and the L/D ratio of the ejector-diffuser system. The entrainment ratio is one of the performance criteria, and it is used in CFD results for comparison. In the case of the circular nozzle, the entrainment ratio is 33%, while for the Chevron nozzle, this value ranges between 29% to 40%.

Secondly, experimental studies are performed with different mass flow rates and test setup configurations. In the initial three tests, the mass flow rates of the primary flow remain constant, while the secondary mass flow rates are adjusted to observe their effects on performance. The subsequent five tests entail modifications to the test setup concerning the L/D ratio and the spool section. This procedure aims to understand the implications of shortening the ejector-diffuser length on the shock train. The findings indicate the importance of an adequate length for the shock train to achieve higher efficiency in the mixing process.

A critical length exists for the shock train to advance successfully. If insufficient space is provided for the shock wave to propagate, its progression becomes constrained, affecting overall efficiency. This phenomenon is evident in the experimental study conducted within this thesis. Specifically, the removal of Diffuser-1 and Diffuser-2 sections reduces the system's vacuum capacity, resulting in an overall decrease in expected performance. The evaluation of vacuum capacity is chosen as the performance criterion for comparing experimental outcomes. In this way, ejector performance is discussed in two perspectives: entrainment and vacuum level.

During the experimental process, a noticeable noise reduction is observed. Unlike other nozzle studies in the High-Altitude Test System, which typically encounter disruptive noise, the ejector-diffuser system experiences less noise attributed to the chevron nozzle.

In conclusion, the Chevron nozzle performs better in mixing the primary and secondary flows than the circular nozzle. While it was expected to achieve higher levels of mixing and vacuum performance, the Chevron nozzle needed to fully meet these expectations under the given geometric and boundary conditions, as evidenced numerically and experimentally. Future studies could explore additional ways to enhance flow mixing. Notably, the acoustic impact of the Chevron nozzle plays a significant role in its applications.

6.2 Future Work

In the future, this topic can be further advanced through the following methods,

- Incorporating acoustic measurement devices into the test setup can facilitate a more in-depth investigation of the acoustic aspects of the chevron nozzle.
- In this study, a cold flow scenario was investigated. However, in future studies, it is possible to explore the effects of heated air by analyzing and testing whether alterations in temperature impact performance.

- Different geometric designs can be developed for the chevron parameters to enhance the entrainment ratio.
- This study can be extended to explore different types of chevron nozzles to enhance mixing performance.
- This study can be performed with transonic condition.

REFERENCES

[1] Li, A., Chen, J., Xi, G., & Huang, Z. (2023). Numerical investigation of the effect of primary nozzle geometries on flow structure and ejector performance for optimal design. Journal of Mechanical Science and Technology, 37(5), 2139–2148.

[2] Aydoğdu, A. (2019). Design of a test setup for altitude simulation (Master's thesis, Fen Bilimleri Enstitüsü).

[3] Comparison of Multiphase Flow Model and Single-Phase Flow Model of Steam Jet Ejector.

[4] Besagni, G., Mereu, R., & Inzoli, F. (2016). Ejector refrigeration: A comprehensive review. Renewable and Sustainable Energy Reviews, 53, 373-407.

[5] Sathiyamoorthy, K., Iyengar, V. S., & Manjunath, P. (2012, December). Annular supersonic ejector design and optimization. In Gas Turbine India Conference (Vol. 45165, pp. 85-93). American Society of Mechanical Engineers.

[6] Besagni, G., Mereu, R., & Inzoli, F. (2016). Ejector refrigeration: A comprehensive review. Renewable and Sustainable Energy Reviews, 53, 373-407.

[7] Gupta, P., Kumar, P., & Rao, S. M. (2022). Artificial neural network based shape optimization of supersonic ejectors in the critical flow regime. Applied Thermal Engineering, 216, 119046.

[8] Huang, B. J., Chang, J. M., Wang, C. P., & Petrenko, V. A. (1999). A 1-D analysis of ejector performance. International journal of refrigeration, 22(5), 354-364.

[9] Meakhail, T. A., Zien, Y., Elsallak, M., & AbdelHady, S. (2008). Experimental study of the effect of some geometric variables and number of nozzles on the performance of a subsonic air—Air ejector. Proceedings of the Institution of Mechanical Engineers, Part A: Journal of Power and Energy, 222(8), 809-818.

[10] Seçkin, C. (2018). Investigation of the effect of the primary nozzle throat diameter on the evaporator performance of an Ejector expansion refrigeration cycle. Journal of Thermal Engineering, 4(3), 1939-1953.

[11] Chen, F., Liu, C. F., & Yang, J. Y. (1994). Supersonic flow in the second-throat ejector-diffuser system. Journal of Spacecraft and Rockets, 31(1), 123-129.

[12] Kong, F., & Kim, H. D. (2016). Optimization study of a two-stage ejector–diffuser system. International Journal of Heat and Mass Transfer, 101, 1151-1162.

[13] Foit, W. (2012). Comparison of single and parallel ejector operation in transcritical R744 cycle (Master's thesis, Institutt for energi-og prosessteknikk).

[14] Sriveerakul, T., Aphornratana, S., & Chunnanond, K. (2007). Performance prediction of steam ejector using computational fluid dynamics: Part 2. Flow structure of a steam ejector influenced by operating pressures and geometries. International Journal of Thermal Sciences, 46(8), 823-833.

[15] Geng, L., Cao, H., Meng, Q., Li, J., & Jiang, P. (2022). Effects of operating conditions and geometries on the performance of nitrogen ejectors for Joule–Thomson cooling. Applied Thermal Engineering, 212, 118557.

[16] Yadav, S. K., Pandey, K. M., Gupta, R., & Kumar, V. (2021). Numerical study for the influences of nozzle exit position, mixing, and diffuser section lengths on performance of CRMC ejector. Journal of the Brazilian Society of Mechanical Sciences and Engineering, 43, 1-14.

[17] Wang, L., Yan, J., Wang, C., & Li, X. (2017). Numerical study on optimization of ejector primary nozzle geometries. International Journal of Refrigeration, 76, 219-229.

[18] Raef, T., Elzahaby, A. A., & Khalil, M. K. (2014, May). Enhancement of propulsion performance through jet noise reduction technologies: a review. In The International Conference on Applied Mechanics and Mechanical Engineering (Vol. 16, No. 16th International Conference on Applied Mechanics and Mechanical Engineering., pp. 1-24). Military Technical College.

[19] Hu, H., Saga, T., Kobayashi, T., & Taniguchi, N. (2002). Mixing process in a lobed jet flow. AIAA journal, 40(7), 1339-1345

[20] Bridges, J., & Brown, C. (2004, May). Parametric testing of chevrons on single flow hot jets. In 10th AIAA/CEAS aeroacoustics conference (p. 2824).

[21] Suvagiya, M., & Sharma, S. D. (2018). On the effect of geometric parameters of chevron nozzle on generation of streamwise vortices in high subsonic jets. In 20th Annual CFD Symposium (pp. 9-10).

[22] Harish Subramanian, G., Nagarjun, C. V., Satish Kumar, K. V., Ashish Kumar, B., Srikanth, V., & Srikrishnan, A. R. (2018). Mixing enhancement using chevron nozzle: studies on free jets and confined jets. Sādhanā, 43, 1-14.

[23] Kanmaniraja, R., Freshipali, R., Abdullah, J., Niranjan, K., Balasubramani, K., & Kumar, V. S. (2014). 3D numerical studies on jets acoustic characteristics of chevron nozzles for aerospace applications. International Journal of Aerospace and Mechanical Engineering, 8(9), 1530-1536.

[24] Kong, F. S., Kim, H. D., Jin, Y., & Setoguchi, T. (2013). Application of Chevron nozzle to a supersonic ejector–diffuser system. Procedia Engineering, 56, 193-200.

[25] Naughton, J., Cattafesta, L., & Settles, G. (1989, July). An experimental study of the effect of streamwise vorticity on supersonic mixing enhancement. In 25th Joint Propulsion Conference (p. 2456).

[26] Zhang, Y., Dong, J., Song, S., Pan, X., He, N., & Lu, M. (2023). Numerical Investigation on the Effect of Section Width on the Performance of Air Ejector with Rectangular Section. Entropy, 25(1), 179.

[27] Kong, F. S., Jin, Y. Z., & Kim, H. D. (2016). Analytical and computational studies on the vacuum performance of a chevron ejector. Shock Waves, 26, 771-788.

[28] Macia, L., Castilla, R., Gamez-Montero, P. J., Camacho, S., & Codina, E. (2019). Numerical simulation of a supersonic ejector for vacuum generation with explicit and implicit solver in openfoam. Energies, 12(18), 3553.

[29] Fu, W., Li, Y., Liu, Z., Wu, H., & Wu, T. (2016). Numerical study for the influences of primary nozzle on steam ejector performance. Applied Thermal Engineering, 106, 1148-1156.

[30] Rand, C. P., Croquer, S., Poirier, M., & Poncet, S. (2022). Optimal nozzle exit position for a single-phase ejector (Experimental, numerical and thermodynamic modelling). International Journal of Refrigeration, 144, 108-117.

[31] Xue, K., Li, K., Chen, W., Chong, D., & Yan, J. (2017). Numerical investigation on the performance of different primary nozzle structures in the supersonic ejector. Energy Procedia, 105, 4997-5004.

[32] Kong, F., Kim, H. D., & Jin, Y. (2013). Computational Study of Supersonic Chevron Ejector Flows. 한국추진공학회지, 17(6), 89-96.

[33] Kotian, S., Jain, N., Methekar, N., & Nikam, S. (2021, December). Turbulent Characteristics of Compressible Jet from a Chevron Nozzle: A Numerical

Study. In Conference on Fluid Mechanics and Fluid Power (pp. 81-86). Singapore: Springer Nature Singapore.

[34] Kong, F., Kim, H. D., Setoguchi, T., & Kim, J. S. (2015). Starting transient flows in a chevron ejector-diffuser system. Journal of Mechanical Science and Technology, 29, 887-892.

[35] Callender, B., Gutmark, E. J., & Martens, S. (2010). Flow field characterization of coaxial conical and serrated (chevron) nozzles. Experiments in fluids, 48, 637-649.

[36] Tide, P. S., & Srinivasan, K. (2010). Effect of chevron count and penetration on the acoustic characteristics of chevron nozzles.

APPENDICES

A. Pressure Data from Experimental Studies

Pressure-time graphs from test chamber of Case 1-8

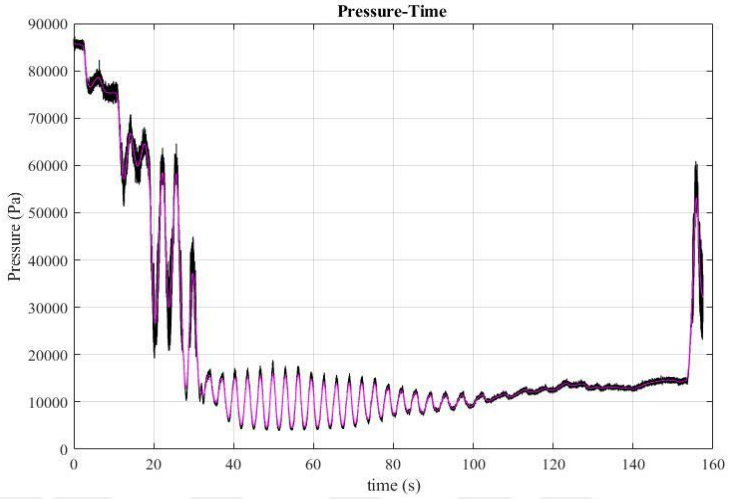

Figure A.1. Pressure-Time graph from P2 point of Case-1

The averaged pressure data from Test Chamber P2 point is taken at the 100th second, and it is approximately 10.1 kPa.

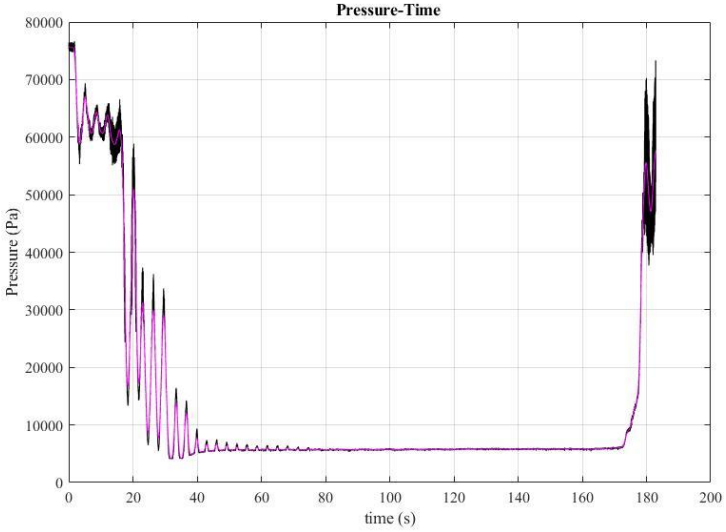

Figure A.2. Pressure-Time graph from P2 point of Case-2

The averaged pressure data from Test Chamber P2 point is taken at the 100th second, and it is approximately 5944 Pa.

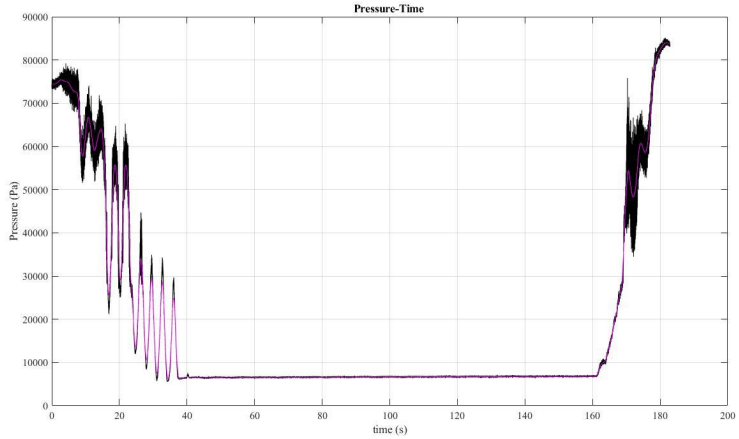

Figure A.3. Pressure-Time graph from P2 point of Case-3

The averaged pressure data from Test Chamber P2 point is taken at the 100th second, and it is approximately 6686 Pa.

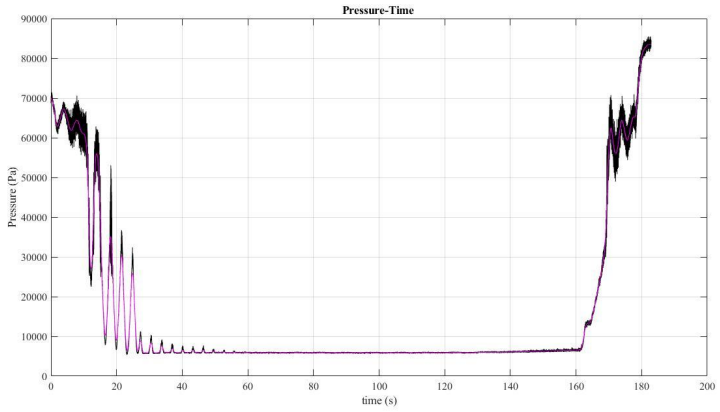

Figure A.4. Pressure-Time graph from P2 point of Case-4

The averaged pressure data from Test Chamber P2 point is taken at the 100th second, and it is approximately 5885 Pa.

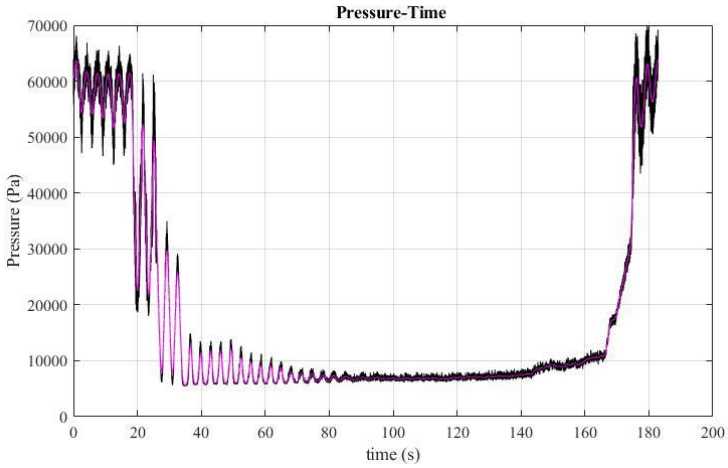

Figure A.5. Pressure-Time graph from P2 point of Case-5

The averaged pressure data from Test Chamber P2 point is taken at the 100th second, and it is approximately 6856 Pa.

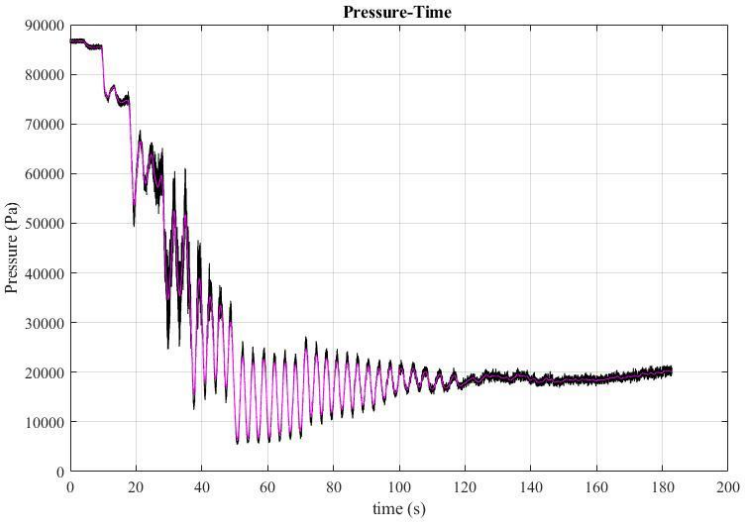

Figure A.6. Pressure-Time graph from P2 point of Case-6

The averaged pressure data from Test Chamber P2 point is taken at the 100th second, and it is approximately 20.7 kPa.

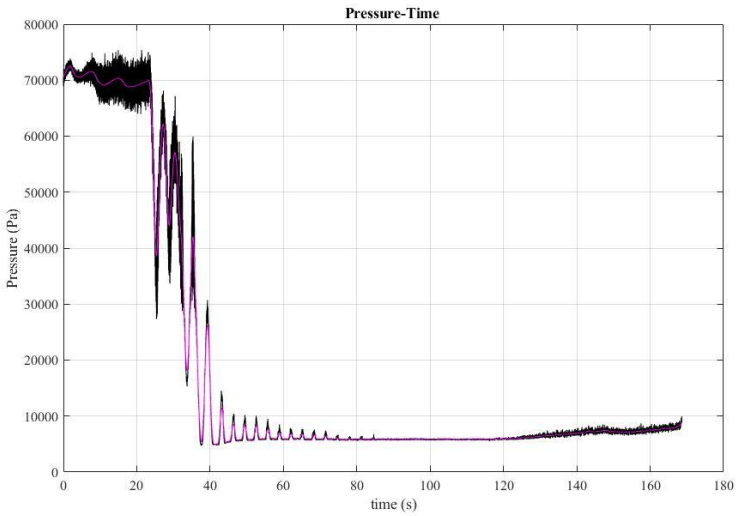

Figure A.7. Pressure-Time graph from P2 point of Case-7

The averaged pressure data from Test Chamber P2 point is taken at the 100th second, and it is approximately 5821 kPa.

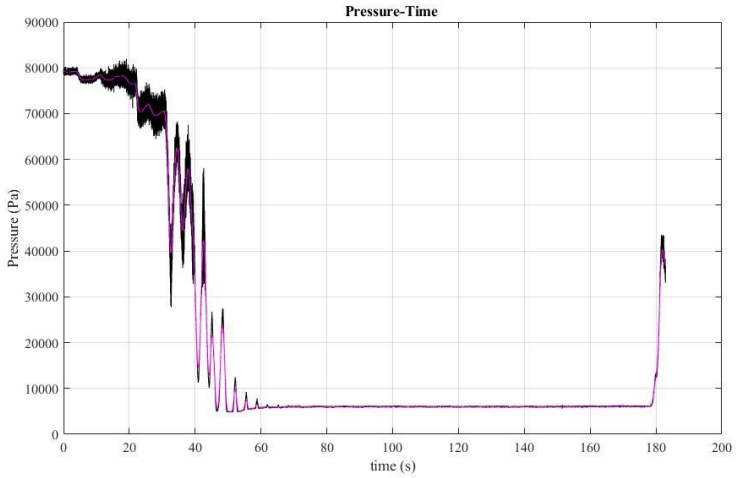

Figure A.8. Pressure-Time graph from P2 point of Case-8

The averaged pressure data from Test Chamber P2 point is taken at the 100th second, and it is approximately 6070 Pa.

Pressure-time graphs from mixing duct of Case 1-8

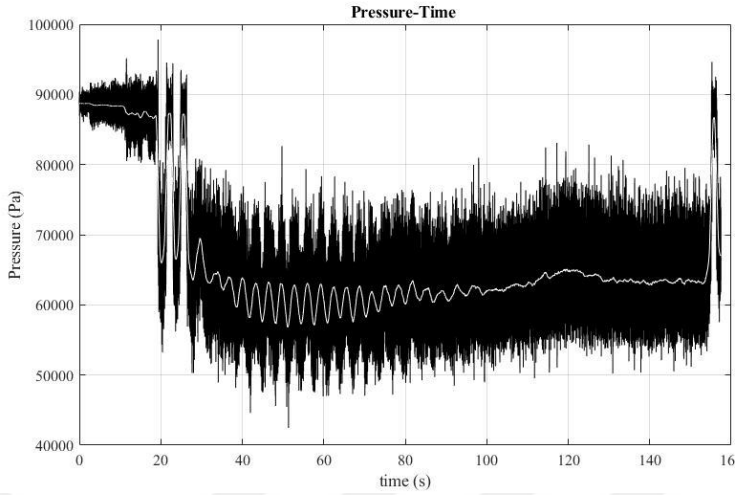

Figure A.9. Pressure-Time graph from P4 point of Case-1

The filtered mean pressure data from the P4 point is taken at the 100th second and is approximately 62.1 kPa.

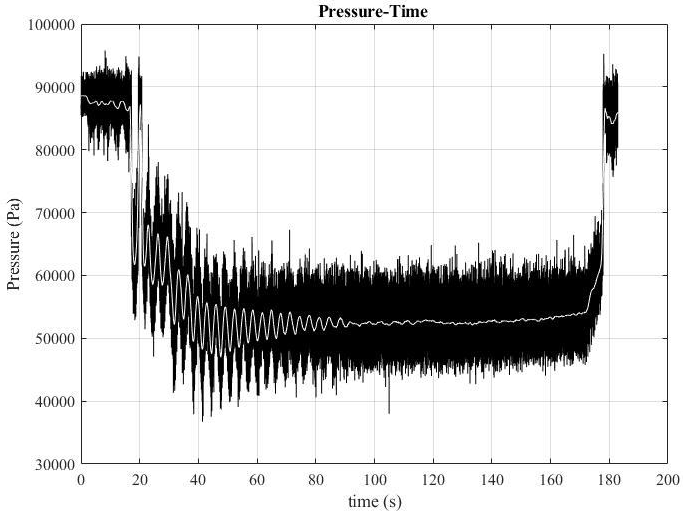

Figure A.10. Pressure-Time graph from P4 point of Case-2

The filtered mean pressure data from the P4 point is taken at the 100th second and is approximately 52.28 kPa.

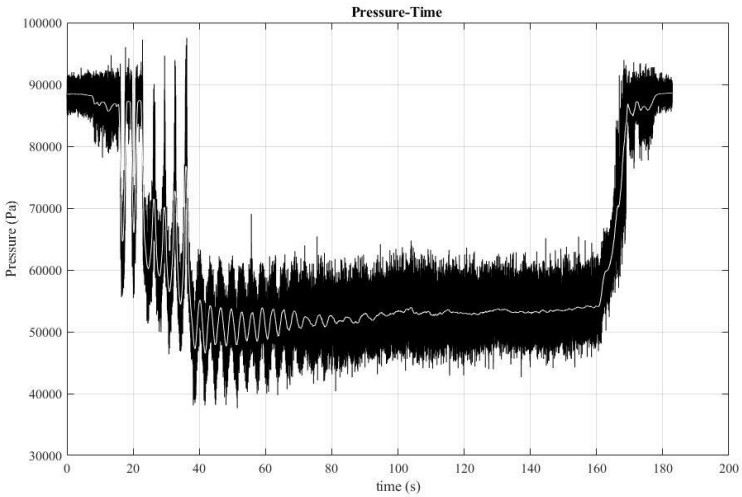

Figure A.11. Pressure-Time graph from P4 point of Case-3

The filtered mean pressure data from the P4 point is taken at the 100th second and is approximately 53.3 kPa.

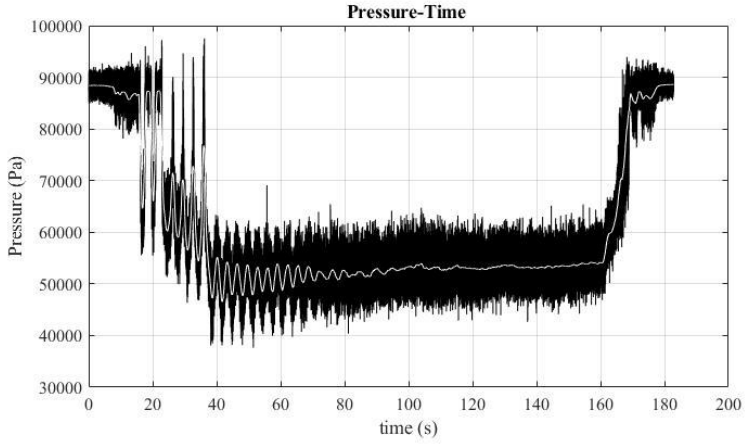

Figure A.12. Pressure-Time graph from P4 point of Case-4

The filtered mean pressure data from the P4 point is taken at the 100th second and is approximately 52.7 kPa.

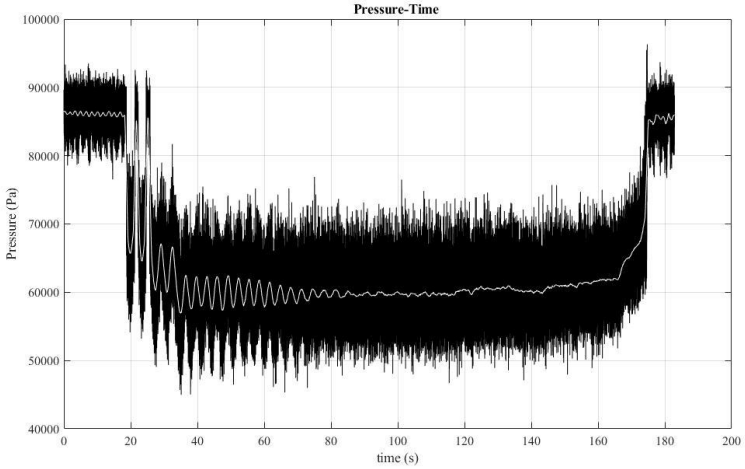

Figure A.13. Pressure-Time graph from P4 point of Case-5

The filtered mean pressure data from the P4 point is taken at the 100th second and is approximately 59.8 kPa.

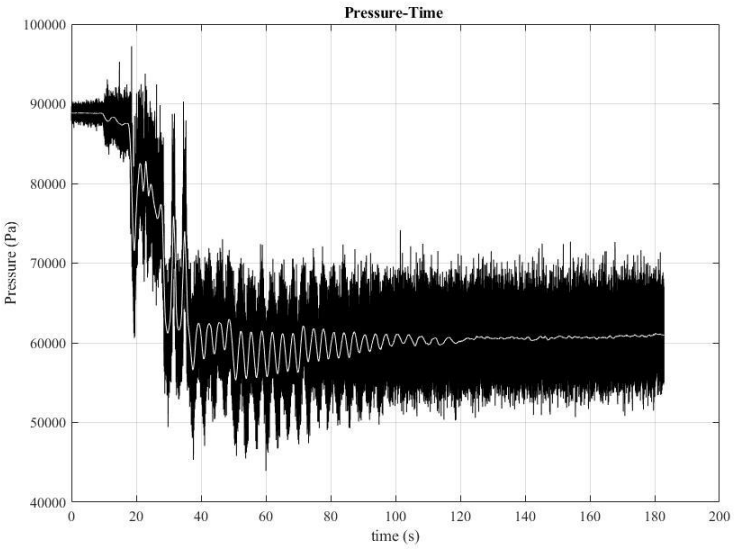

Figure A.14. Pressure-Time graph from P4 point of Case-6

The filtered mean pressure data from the P4 point is taken at the 100th second and is approximately 61 kPa.

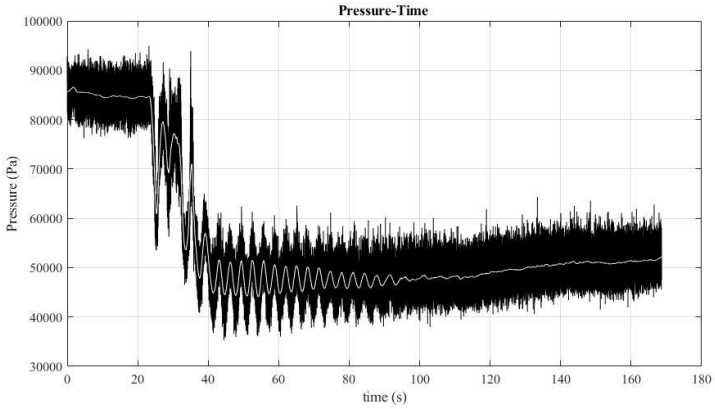

Figure A.15. Pressure-Time graph from P4 point of Case-7

The filtered mean pressure data from the P4 point is taken at the 100th second and is approximately 48.1 kPa.

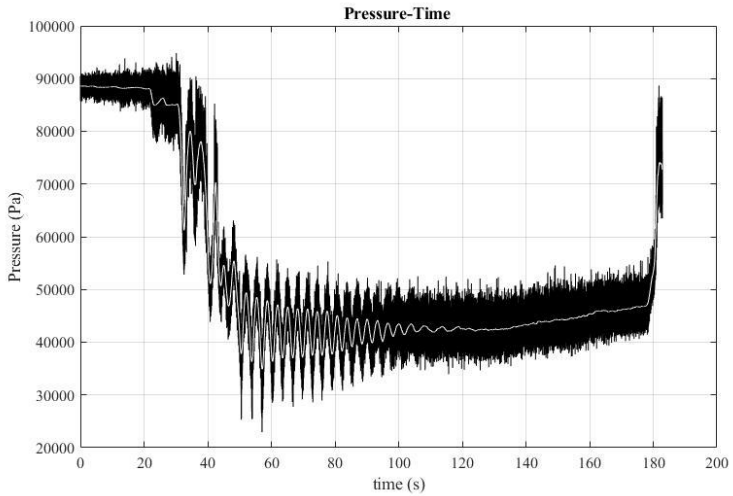

Figure A.16. Pressure-Time graph from P4 point of Case-8

The filtered mean pressure data from the P4 point is taken at the 100th second and is approximately 43.1 kPa.

B. Pressure Result from Additional Experiment

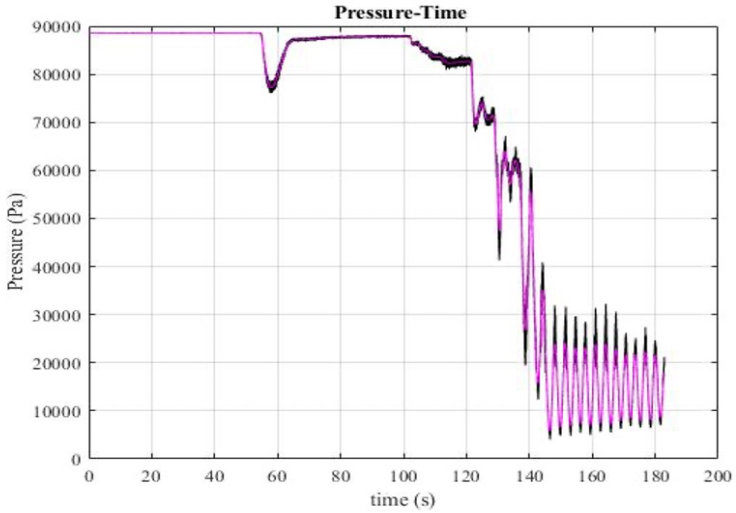

Figure B.1. Pressure-Time graph from P1 point

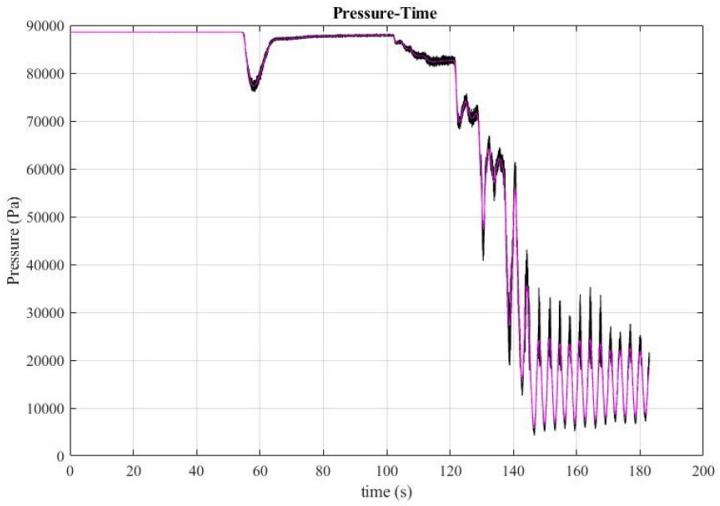

Figure B.2. Pressure-Time graph from P2 point

The filtered mean pressure data from Test Chamber P1 point was approximately 19266.43 Pascal. The filtered mean pressure data from the Test Chamber P2 point was approximately 19527.37 Pascal.